
The Quantization Benefits of Residual-Free Transformers

Yiping Ji^{1*}Mahalakshmi Sabanayagam^{1*}Peyman Moghadam²Hemanth Saratchandran¹Simon Lucey¹¹ Australian Institute for Machine Learning, Adelaide University ² DATA61, CSIRO

Abstract

Large-scale transformer training and deployment are increasingly constrained by the transfer of activations, gradients, and optimizer states across accelerators. Low-bit quantization offers a natural remedy, but transformer activations are often heavy-tailed and outlier-dominated, making simple quantization highly lossy. We show that this difficulty is not only a property of the quantizer, but also of the architecture. Specifically, residual connections can drive transformer activations away from Gaussianity during training. Using controlled comparisons between residual and residual-free transformers, we demonstrate that this effect leads to substantially higher quantization error and accuracy degradation at low precision in residual models. We explain the phenomenon through an excess kurtosis analysis, showing that residual mixing can amplify non-Gaussianity, whereas dense mixing in residual-free contracts non-Gaussianity. We then show that residual-free transformers can be made trainable using orthogonal initialization, spectral or second-order optimization, and depth-aware scaling of attention temperature. In language tasks, while there is a small drop in full precision performance, these models retain near-Gaussian activations and exhibit significantly improved robustness to low-bit quantization. Our results identify an *accuracy-compressibility trade-off* in transformer design and motivate architecture-level approaches to quantization-friendly foundation models.

1 Introduction

The recent success of large foundation models such as GPT-4, PaLM, and LLaMA has been enabled by aggressive scaling of model size, data, and compute [Hoffmann et al., 2022]. However, this scaling trend has made training increasingly constrained by systems efficiency rather than model design alone. State-of-the-art models are now trained across thousands of accelerators using data, tensor, pipeline, and optimizer-state parallelism [Shoeybi et al., 2019, Huang et al., 2019, Narayanan et al., 2019, Rajbhandari et al., 2020, Xu et al., 2021]. While these approaches enable training extremely large models, they also introduce substantial communication overhead. As models are distributed across more devices, more training time and energy are spent transferring activations, gradients, and optimizer states between devices instead of doing local computation. Consequently, the efficiency of large-scale training is increasingly governed by how effectively these tensors can be communicated, and in particular by how well they can be compressed without losing performance. This gives rise to a central challenge in distributed training where *communication overhead can dominate computation*.

*Equal contribution. Emails: yiping.ji@adelaide.edu.au, mahalakshmi.sabanayagam@adelaide.edu.au

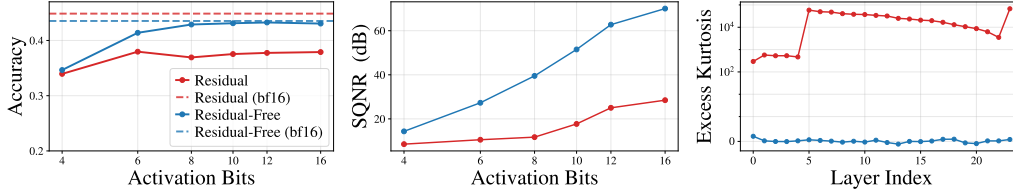


Figure 1: **Residual-free transformers remain near-Gaussian and quantization-robust.** On 24-layer models trained in bf16 precision, the residual-free model with *orthogonal initialization and KL Shampoo* achieves performance comparable to the residual one on 8 downstream tasks and retains substantially high accuracy under aggressive quantization (int) of activations and 8-bit weights, while the residual model degrades sharply (**left**). This gap is explained by a higher signal-to-quantization-noise ratio (SQNR) (**middle**) and near-Gaussian activations measured by excess kurtosis (near-zero indicates near-Gaussian in the fourth-moment sense) across layers (**right**), whereas residual models develop heavy-tailed activations.

A major response to tackle this problem has been low-precision training and quantization. FP8 training and low-bit quantization methods have substantially reduced the memory and communication cost of large models [Mickeyevicius et al., 2022, Zandieh et al., 2025]. However, the success of these methods often depends on increasingly specialized machinery beyond simple low-precision, such as mixed-precision outlier channels, per-channel or per-token scaling, clipping calibration, equivalent transformations, and layerwise reconstruction. A key reason is that transformer activations are often non-Gaussian, heavy-tailed, and dominated by a small number of outliers, making naive low-bit quantization highly lossy [Li et al., 2020]. Prior work has linked these structured activation outliers and large activation ranges to residual connections, attention, normalization, and training-dynamics effects [Bondarenko et al., 2021, 2023, Dettmers et al., 2022, Xiao et al., 2023, Wei et al., 2023, He et al., 2024]. This suggests that quantization difficulty is partly architectural, determined by whether the tensors being communicated are inherently poorly suited for compression.

Motivated by this architectural view of quantization difficulty, we take a different perspective on post-training quantization. Rather than asking how to compensate for pathological activations after they appear, we ask **which architectural mechanisms give rise to them, and whether they can be mitigated at the source**. Complementing prior work on activation outliers, we isolate the role of residual connections through controlled residual versus residual-free comparisons. We show that residual connections, while central to optimization in transformers, can drive activations away from Gaussianity during training, making them increasingly difficult to quantize. Whereas, *residual-free transformers with orthogonal initialization [Saxe et al., 2014] and second-order optimization, such as Muon [Jordan et al., 2024], SOAP [Vyas et al., 2025], and Shampoo [Gupta et al., 2018, Lin et al., 2025], maintain nearly Gaussian-like activations across layers and training time*. This statistical difference has direct consequences for low precision. As shown in Figure 1, under simple uniform quantization of activations and weights, residual models incur substantially higher accuracy degradation and information loss than their residual-free counterparts. The excess kurtosis measurements confirm that this gap is associated with heavier-tailed, non-Gaussian activations. These results reveal an accuracy–compressibility tradeoff in residual models as well as motivate residual-free transformer as a potential architecture-level route to quantization-friendly foundation models.

While the preservation of near-Gaussian activations in residual-free networks is promising for quantization, it remains a practical challenge to train these networks compared to their residual counterparts, as skip connections were introduced precisely to stabilize optimization in deep networks. A growing body of work has studied how to recover the optimization benefits of residual connections without explicit skip connections through different parameterizations and initializations [Hardt and Ma, 2017, Xiao et al., 2018, He et al., 2023]. Recent work on residual-free transformers further shows that suitable initialization can substantially close the optimization and performance gaps to residual architectures [Ji et al., 2026]. Building on this line of work, we further explore the trainability aspects of residual-free transformers and find that orthogonal initialization, spectral or second-order optimization, and appropriate depth-aware scalings of attention temperature can effectively train residual-free transformers. Crucially, these models retain near-Gaussian activation statistics throughout training, leading to substantially better low-bit quantization than residual transformers. Our **contributions** are summarized as follows:

1. Residual connection is a controllable source of quantization-unfriendly activation statistics.

We identify residual connections as a key architectural source of activation non-Gaussianity in transformers. Across controlled residual versus residual-free comparisons, we show that residual models develop heavy-tailed activations during training, whereas residual-free models can preserve near-Gaussian activations when paired with orthogonal initialization and second-order optimization.

2. Excess kurtosis analysis explains why residual mixing amplifies non-Gaussianity. We provide an analysis under simplified settings showing that residual mixing preserves and can amplify excess kurtosis, whereas dense mixing contracts it. Our analysis shows that preserving Gaussianity requires both appropriate initialization and optimization, and cannot be achieved by either alone (Section 3).

3. A practical residual-free training recipe yields quantization-friendly transformers. We develop a practical recipe for training residual-free transformers in Section 4 combining orthogonal initialization, second-order optimization, and depth-aware scaling of attention temperature. In Section 5, we show that while there is a small drop in full-precision performance, these models exhibit substantially higher robustness to simple uniform quantization in language tasks. These results reveal an *accuracy-compressibility trade-off* between residual and residual-free transformers.

2 Related Work

We focus on works most directly related to residual-free transformers, activation outliers, and quantization. A broader discussion appears in Section A.

Residual-free transformers. [He et al., 2023] study training transformers without residual connections or normalization and show that they suffer from rank collapse, where the kernel matrix converges to rank one with depth. They modify self-attention to preserve well-behaved kernels at initialization, but report substantially more training steps (roughly 5 times) to match residual baselines. Further, Ji et al. [2026] show that residual-free transformers can train as efficiently as residual models using a principled initialization of the self-attention block, without architectural changes and while remaining compatible with FlashAttention [Dao et al., 2022, Dao, 2024]. However, their method still struggles to scale to deeper networks, for example, beyond 12 layers.

Quantization and activation outliers in transformers. Many prior works have identified outliers in transformer activations and studied their effect on quantization. [Bondarenko et al., 2021] identify that transformer activations exhibit structured outliers that are difficult to represent with low-bit fixed-point formats, while [Bondarenko et al., 2023] links these outliers to attention heads. He et al. [2024] and Nrusimha et al. [2024] analyze how architectural and optimization choices influence the emergence of outlier features during training. To address these issues, low-precision FP8 training and low-bit quantization are introduced. For example, LLM.int8() [Dettmers et al., 2022] uses mixed-precision decomposition to isolate outlier channels, SmoothQuant [Xiao et al., 2023] shifts activation outlier difficulty into weights through equivalent transformations, and methods such as QLoRA [Dettmers et al., 2023] and TurboQuant [Zandieh et al., 2025] adopt specialized scaling, clipping, or reconstruction techniques. Our work takes a complementary perspective. Instead of compensating for outliers after they arise, we study whether architecture and optimization can produce activation statistics that are easier to quantize without any outlier-handling methods in a controlled setting.

3 Analysis of Activations of Residual and Residual-Free Transformers

3.1 Setup and Preliminaries

We compare residual and residual-free transformers through the evolution of their layerwise activation statistics. We give only the notation needed for the main argument here, and defer a complete architectural specification to Section B.

Notation. We write vectors and matrices in boldface. For $\mathbf{v} \in \mathbb{R}^d$, v_i denotes its i -th coordinate. For $\mathbf{M} \in \mathbb{R}^{m \times n}$, M_{ij} denotes its (i, j) -th entry. Unless otherwise stated, $\|\cdot\|$ denotes the Euclidean norm for vectors and the spectral norm for matrices, and \mathbf{I}_d denotes the d -dimensional identity matrix. For a function f , we use ∇f to denote its gradient.

Residual and residual-free blocks in transformer. Let $\mathbf{X}_\ell \in \mathbb{R}^{T \times d}$ denote the token representation at layer ℓ , where T is the sequence length and d is the model dimension. Each transformer block

consists of a self-attention map $\text{SA}(\cdot)$ and a position-wise feedforward map $\text{MLP}(\cdot)$, both applied to normalized inputs through $\text{norm}(\cdot)$. For a residual transformer,

$$\mathbf{Y}_\ell = \mathbf{X}_{\ell-1} + \text{SA}(\text{norm}(\mathbf{X}_{\ell-1})), \quad \mathbf{X}_\ell = \mathbf{Y}_\ell + \text{MLP}(\text{norm}(\mathbf{Y}_\ell)). \quad (1)$$

The residual-free counterpart removes the additive skip paths,

$$\mathbf{Y}_\ell = \text{SA}(\text{norm}(\mathbf{X}_{\ell-1})), \quad \mathbf{X}_\ell = \text{MLP}(\text{norm}(\mathbf{Y}_\ell)). \quad (2)$$

This distinction, the presence or absence of the additive identity path, is the architectural feature we isolate in the analysis. Here $\text{norm}(\cdot)$ denotes either Layer Normalization Ba et al. [2016] or RMS Normalization [Zhang and Sennrich, 2019], and serves to control the scale of the input to each sublayer. The self-attention operation $\text{SA}(\cdot)$ for any input \mathbf{X} is defined as

$$\text{SA}(\mathbf{X}) = \mathbf{A}\mathbf{V}\mathbf{W}^O,$$

where $\mathbf{Q} = \mathbf{X}\mathbf{W}^Q$, $\mathbf{K} = \mathbf{X}\mathbf{W}^K$, $\mathbf{V} = \mathbf{X}\mathbf{W}^V$, and the attention matrix is $\mathbf{A} = \text{softmax}(\frac{1}{\sqrt{d}}\mathbf{Q}\mathbf{K}^\top)$. The parameter matrices $\mathbf{W}^Q, \mathbf{W}^K, \mathbf{W}^V, \mathbf{W}^O \in \mathbb{R}^{d \times d}$ are learnable. In practice, $\text{SA}(\cdot)$ is multi-head attention with h heads and has the form

$$\text{SA}(\mathbf{X}) = \text{Concat}(\mathbf{A}_1\mathbf{V}_1, \dots, \mathbf{A}_h\mathbf{V}_h)\mathbf{W}^O,$$

where \mathbf{A}_i are attention matrices with projection matrices $\mathbf{W}_i^Q, \mathbf{W}_i^K, \mathbf{W}_i^V \in \mathbb{R}^{d \times d_h}$, $d_h = \frac{d}{h}$ and \mathbf{W}^O is the output projection. The MLP block has the form

$$\text{MLP}(\mathbf{X}) = \phi(\mathbf{X}\mathbf{W}^U)\mathbf{W}^D,$$

where ϕ is a pointwise nonlinearity such as GELU, and $\mathbf{W}^U \in \mathbb{R}^{d \times d_f}$ and $\mathbf{W}^D \in \mathbb{R}^{d_f \times d}$ are learnable parameters. Thus, at the level of a single coordinate or token, each sublayer repeatedly applies a nonlinear transformation and then mixes coordinates through matrices such as \mathbf{W}^O and \mathbf{W}^D . Our analysis focuses on how this mixing changes higher-order activation statistics, and how the additive residual path changes that evolution.

Initialization. We analyze standard variance-preserving initializations, such as Xavier (Glorot) [Glorot and Bengio, 2010] or Kaiming [He et al., 2015], and orthogonal initialization [Saxe et al., 2014]. The key property for our analysis is that orthogonal mixing preserves norms and avoids the row-norm and singular-value fluctuations present in dense Gaussian initialization.

Optimization models. To reason about training dynamics of loss \mathcal{L} while keeping the analysis tractable, we use two stylized update rules. First, *sign gradient descent* (GD) [Bernstein et al., 2018],

$$\mathbf{W}_{t+1} = \mathbf{W}_t - \eta \text{sign}(\nabla \mathcal{L}(\mathbf{W}_t)), \quad (3)$$

where $\eta > 0$ is the learning rate and the sign function is applied elementwise. It serves as a simplified model of coordinate-wise adaptive first-order methods such as Adam [Kingma and Ba, 2015] and AdamW [Loshchilov and Hutter, 2019]. Second, *spectral gradient descent* updates a matrix in the polar direction of its gradient. If $\nabla \mathcal{L}(\mathbf{W}_t) = \mathbf{U}_t \mathbf{S}_t \mathbf{V}_t^\top$, then

$$\mathbf{W}_{t+1} = \mathbf{W}_t - \eta \mathbf{U}_t \mathbf{V}_t^\top. \quad (4)$$

This update is a tractable proxy for matrix-preconditioned or spectral second-order methods such as Shampoo [Gupta et al., 2018], Muon [Jordan et al., 2024], SOAP [Vyas et al., 2025], and KL Shampoo [Lin et al., 2025]. We emphasize that these update rules are not exact models of AdamW, Muon, SOAP, or KL Shampoo. They isolate the geometric distinction relevant to our analysis, in which coordinatewise updates can introduce anisotropy, whereas matrix-normalized or preconditioned updates can better preserve near-isometry induced by orthogonal initialization.

3.2 Theoretical Analysis of Layerwise Activation Distributions

We first establish that normalization is necessary to control second moments in both residual and residual-free transformers. We then analyze the higher-order statistics, thereby the distribution of activations, using excess kurtosis, which characterizes the tailedness of a distribution. The theoretical results below are intentionally idealized. They are meant to isolate the fourth-moment effect of dense mixing and residual addition, not to fully model all dependencies present in trained transformers.

Variance dynamics without normalization. We consider the layerwise recursions defined in Section 3.1 and analyze the behavior of the variance across depth.

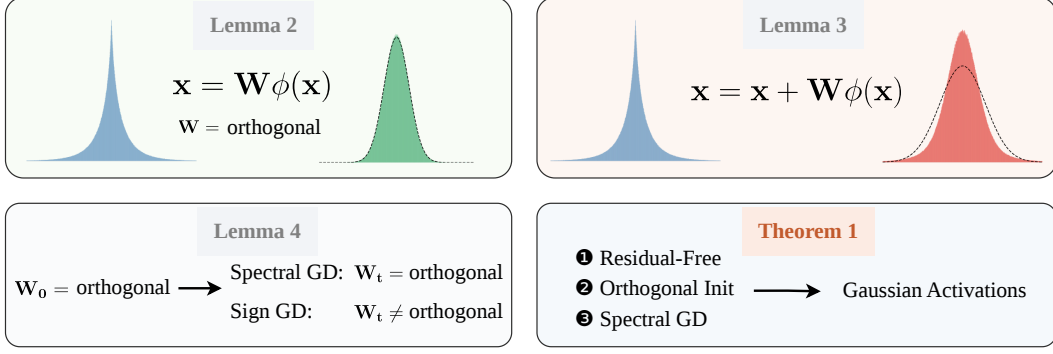


Figure 2: **Mechanism of Gaussianization vs accumulation in transformers.** Residual-free dense mixing contracts excess kurtosis γ and drives activations toward Gaussianity (Lemma 2), while residual addition preserves non-Gaussian components (Lemma 3). When weight matrices remain near-isometric during training, for example, under orthogonal initialization and spectral updates (Lemma 4), residual-free models preserve near-Gaussian activations, whereas residual ones tend to be heavy-tailed (Theorem 1). This difference explains the robustness gap in low-bit quantization.

Lemma 1 (Normalization controls variance collapse and growth). *Consider the residual and residual-free update in Eqs. (1) and (2) without normalization, that is, $\text{norm}(\mathbf{X}) = \mathbf{X}$. Assume coordinates of \mathbf{X}_ℓ are centered with variance q_ℓ , and weight matrices are variance-preserving. Then,*

- **Residual-free case:** *The variance of $\mathbf{X}_{\ell+1}$, $q_{\ell+1} = cq_\ell$ with $c < 1$ for common nonlinearities that contracts the input. Hence, the variance of deep layers, $q_L \rightarrow 0$ exponentially with depth.*
- **Residual case:** *The variance of $\mathbf{X}_{\ell+1}$, $q_{\ell+1} = (1+c)q_\ell$ with $c > 0$ under weak correlation, so q_L grows exponentially with depth.*

Normalization $\text{norm}(\cdot)$ prevents both variance collapse and growth by rescaling the input to each sublayer so that the variance remains $\mathcal{O}(1)$ across layers.

Residual-free networks suffer variance collapse, while residual networks exhibit variance explosion in the absence of normalization, even when weights are variance preserving (proof in Section C.1). While this lemma is not used as a quantitative prediction for trained normalized transformers, it motivates the use of $\text{norm}(\cdot)$ to maintain the variance and to condition the kurtosis analysis on normalized inputs and focus on higher-order statistics. All proofs are provided in Section C.

Excess kurtosis as a measure of non-Gaussianity. We use excess kurtosis as a scalar proxy for deviation from Gaussianity. While excess kurtosis does not uniquely characterize a distribution, it provides a simple and tractable measure of tail heaviness and deviation from Gaussian fourth moments. We therefore use it together with negentropy and histograms in the experiments. Figure 2 outlines our analysis and summarizes the two competing mechanisms that govern the activation statistics. Dense mixing without residual connections acts as a *Gaussianizing* operator, contracting excess kurtosis. In contrast, residual addition introduces an *accumulating* path that preserves and can amplify non-Gaussian components. The extent to which these effects manifest in deep networks further depends on whether the weight matrices remain close to isometric during training.

Definition 1 (Excess kurtosis). *Let v be a random variable with mean μ and variance σ^2 . Its excess kurtosis is $\gamma_v = \frac{\mathbb{E}[(v-\mu)^4]}{(\mathbb{E}[(v-\mu)^2])^2} - 3$.*

For standardized variables, $\gamma_v = \mathbb{E}[v^4] - 3$. Gaussian distributions satisfy $\gamma_v = 0$. Thus, values of γ_v close to 0 indicate that v is close to Gaussian in the fourth-moment sense. We now characterize how excess kurtosis evolves across layers, first for a single layer residual-free connections.

Lemma 2 (Dense orthogonal mixing contracts excess kurtosis). *Let $y_j = \sum_{i=1}^d W_{ij}\phi(x_i)$ where $\mathbf{x} \in \mathbb{R}^d$ has independent coordinates and each random variable x_i is centered and has isotropic variance similar to the output from $\text{norm}(\cdot)$, and $\mathbf{W} \in \mathbb{R}^{d \times d}$. Assume further that for each x_i has*

the same excess kurtosis γ_x and \mathbf{W} is dense orthogonal. Then excess kurtosis of y_j , γ_y is

$$\gamma_y = \mathcal{O}\left(\frac{\gamma_x}{d}\right).$$

First, the independence assumptions should be interpreted as mean-field approximations to the post-normalization statistics since normalizations introduce dependencies across coordinates [Xiong et al., 2020]. Lemma 2 is a fourth-moment version of a central-limit effect. When no coordinate dominates the mixing row and cross-coordinate dependence is weak, the fourth cumulants are averaged across many coordinates, yielding a $1/d$ contraction. For ReLU/GELU, the coordinatewise excess kurtosis is $\mathcal{O}(1)$ under Gaussian inputs, and for softmax, this remains true only in a non-saturated regime, which is maintained by orthogonal \mathbf{Q} and \mathbf{K} , and temperature scaling (proof in Section C.6). While Gaussian weights can also produce a local shrinkage effect, orthogonal initialization provides stronger geometric control over the mixing process, which is crucial for maintaining this behavior across layers as shown in Section C.3.

Lemma 3 (Residual addition prevents $1/d$ excess kurtosis contraction). *Let the residual update be $y_j = x_j + \sum_{i=1}^d \phi(x_i)W_{i,j}$ where $\mathbf{x} \in \mathbb{R}^d$ has independent coordinates and each random variable x_i is centered and has isotropic variance similar to the output from $\text{norm}(\cdot)$, and $\mathbf{W} \in \mathbb{R}^{d \times d}$ have i.i.d. Gaussian entries $\mathcal{N}(0, \frac{1}{d})$ independent of \mathbf{x} . Then the excess kurtosis of y_j is*

$$\gamma_y = \mathcal{O}\left(\gamma_x + \frac{1}{d}\right).$$

The key difference from Lemma 2 is the presence of the identity path. The residual update directly preserves the original coordinate x_j , and does not provide the same $1/d$ averaging effect that drives Gaussianization. As a result, excess kurtosis does not contract across layers and instead remains on the order of the input kurtosis. While we state the result for Gaussian \mathbf{W} for analytical convenience, similar behavior holds for more general weight matrices (proof in Section C.5).

Lemmas 2 and 3 describe how kurtosis propagates under a specific weight matrix. The contraction in the residual-free case relies on maintaining effective dense mixing during training. Therefore, it is critical to analyze whether the weight matrices maintain the characteristics during training.

Lemma 4 (Spectral GD preserves near-isometry, whereas sign GD destroys isometry faster). *Let \mathbf{W}_{t-1} satisfy near-isometry and η be the learning rate. Then the spectral update in Eq. (4) follows*

$$\|\mathbf{W}_t \mathbf{W}_t^\top - \mathbf{I}\|_2 \leq \mathcal{O}(\eta), \tag{5}$$

and the sign update in Eq. (3) follows

$$\|\mathbf{W}_t \mathbf{W}_t^\top - \mathbf{I}\|_2 \leq \mathcal{O}(\eta\sqrt{d} + \eta^2 d). \tag{6}$$

This stylized comparison suggests why matrix-normalized or second-order optimizers may better preserve the dense near-isometric geometry needed for kurtosis contraction. In contrast, sign-like updates suggest why coordinatewise updates such as AdamW introduce anisotropy much more rapidly, degrading the mixing structure and weakening Gaussianization even in residual-free structure. Refer to Section C.4 for proofs. Putting together, we obtain Theorem 1.

Theorem 1 (Near-Gaussian activations). *Under the independence, dense-mixing, and near-isometry assumptions above, the combination of **residual-free + orthogonal initialization + spectral-type optimizer** admits a near-Gaussian activations layerwise. The qualitative regimes predicted by the analysis are summarized below, where \checkmark indicates near-Gaussian activations and \times indicates non-Gaussian activations.*

Architecture	Optimizer	Gaussian init.	Orthogonal init.
Residual	Sign GD	\times	\times
Residual	Spectral GD	\times	\times
Residual-free	Sign GD	\times	\times
Residual-free	Spectral GD	\times	\checkmark

Our analysis identifies a regime in which residual-free transformers can maintain near-Gaussian activations throughout training. This regime requires *both* dense orthogonal mixing at initialization and optimization dynamics that approximately preserve this geometry, such as spectral or second-order updates. Either component alone is insufficient. In contrast, residual architectures generally lack the same Gaussianizing mechanism, since the skip path preserves higher-order moments. This architectural difference helps explain why the two model families behave differently under simple uniform low-bit quantization.

Near-Gaussian activation is a three-part recipe: Residual-free, orthogonal initialization, and second-order optimization. All three are necessary.

4 Practical Recipe to Train Deep Residual-Free Transformers

While residual-free architectures offer favorable activation statistics for compression, they are typically substantially harder to optimize than their residual counterparts. Residual connections were introduced precisely to stabilize training in deep networks [He et al., 2016, Srivastava et al., 2015], and removing these connections can lead to poor signal propagation, slower convergence, and degraded final performance. A long line of work has therefore studied how to train deep networks without explicit residual connections and makes it clear that residual-free training is possible only when signal propagation is carefully controlled through appropriate initialization [Saxe et al., 2014, Xiao et al., 2018] and parameterization [Hardt and Ma, 2017, Zagoruyko and Komodakis, 2017, He et al., 2015]. While [Ji et al., 2026] achieved competitive performance for residual-free transformers with careful initialization of attention weights that maintain a well-conditioned Jacobian, it still remains a challenge to train very deep residual-free transformers. These works show that the trainability gap can be narrowed, but also that residual-free training requires careful control of the network geometry.

In this section, we develop a simple and effective recipe for training residual-free transformers, building on the insights we derived through our analysis in Section 3.2. The key challenge is to preserve the Gaussianizing effect of dense mixing while maintaining stable optimization in the absence of residual connections. We achieve this through three components: (i) orthogonal initialization to preserve isotropic mixing, (ii) spectral or second-order optimization to maintain this geometry during training, and (iii) depth-aware scaling of attention temperature to stabilize signal propagation across layers. The goal is to maintain the well-conditioned, isotropic mixing needed for trainability while retaining the near-Gaussian activations that make residual-free models quantization-friendly. We note that this is not intended to be a unique strategy, but we found it to be effective in our experiments.

(i) **Orthogonal initialization.** We begin with an initialization that ensures each layer performs well-conditioned dense mixing. Following [Ji et al., 2026], we initialize the $\mathbf{W}^V, \mathbf{W}^O$ to be scaled orthogonal matrix, such that $\mathbf{W}^V \mathbf{W}^O \approx \alpha_{VO} \mathbf{I}$, where α_{VO} is a hyperparameter. We initialize \mathbf{W}^U and \mathbf{W}^D to be scaled-corrected uniform orthogonal (SUO) distribution [Martens et al., 2021], such that $\mathbf{W}^U \mathbf{W}^{U\top} \approx \alpha_U \mathbf{I}$ and $\mathbf{W}^D \mathbf{W}^{D\top} \approx \alpha_D \mathbf{I}$. For attention, we initialize each head with $\mathbf{W}_i^Q \approx \mathbf{W}_i^K$ to be scaled semi-orthogonal matrix, such that $\mathbf{W}_i^Q \mathbf{W}_i^{K\top} \approx \alpha_{QK} \mathbf{I}$, where α_{QK} is a hyperparameter. This ensures that, at initialization, each layer performs well-conditioned dense mixing, which is critical for maintaining stable signal propagation in the absence of residual paths.

(ii) **Spectral or second order optimization.** We pair orthogonal initialization with spectral-type optimizations that preserve isotropy during training, whereas sign-like updates introduce anisotropy at a rate that grows with dimension (Lemma 4). Since the Gaussianizing effect in Lemma 2 relies on dense, well-conditioned mixing, preserving near-isometry is essential for maintaining stable activation statistics. In practice, we therefore use Muon, SOAP, KL Shampoo optimizers, which empirically show to maintain near-Gaussianity of activations, as discussed in Section 5.

(iii) **Depth-aware scaling of attention temperature.** Even with appropriate initialization and optimization, residual-free models require careful scaling to prevent signal attenuation or amplification across layers. Therefore, we introduce a scaling that modifies the attention to $\text{softmax}\left(\frac{\tau_\ell}{\sqrt{d}} \mathbf{QK}^\top\right)$, where $\tau_\ell = \beta^{-\ell}$ with $\beta > 1$ is a depth-dependent temperature scaling. This controls the sharpness of attention distributions and prevents saturation or collapse of attention patterns as depth increases.

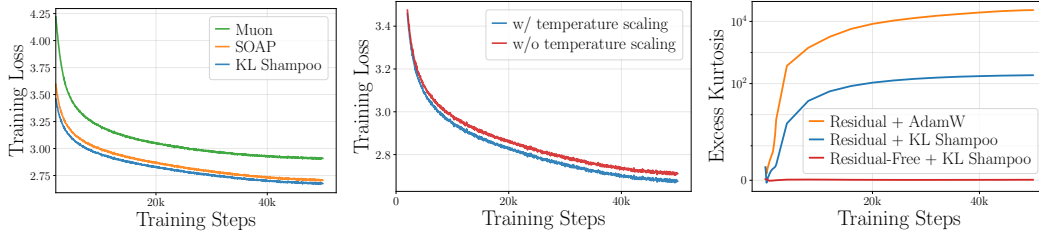


Figure 3: Comparison of optimizers in Residual-Free transformers (**Left**). Temperature scaling improves training convergence (**Middle**). Comparison of excess kurtosis over training (**Right**).

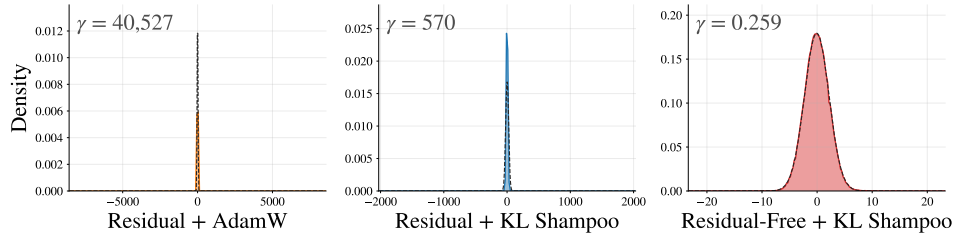


Figure 4: Activation histograms for layer 16 at 50k step showing excess kurtosis (γ). **Left and middle:** residual transformers show heavy-tailed, non-Gaussian activations with large excess kurtosis exhibiting sharp peaks and extreme outliers, leading to high quantization error. **Right:** residual-free transformers show near-Gaussian activations ($\gamma = 0.259$), thus resulting in low quantization error.

Together, these components provide a simple recipe for training residual-free transformers. In the experiments that follow in Section 5, we show that this combination enables residual-free transformers to retain activation statistics that are substantially more favorable for low-precision quantization.

5 Experimental Results

We evaluate both residual and residual-free transformers on language tasks. After training, we quantize model parameters and activations from BF16/full precision to low-bit integer formats and report downstream accuracy. Detailed experimental configurations are provided in Section D. We pretrain all models on FineWeb-Edu [Penedo et al., 2024] for 50k steps using a batch size of 512 sequences, sequence length of 512, and the next-token prediction objective. We evaluate the resulting models on eight commonsense reasoning benchmarks: *arc_c*, *arc_e* [Clark et al., 2018], *boolq* [Clark et al., 2019], *hellaswag* [Zellers et al., 2019], *openbookqa* [Mihaylov et al., 2018], *piqa* [Bisk et al., 2020], *social_iqa* [Sap et al., 2019], and *winogrande* [Sakaguchi et al., 2021]. Residual transformers are trained using AdamW and KL Shampoo, while residual-free transformers are trained primarily with KL Shampoo and orthogonal initialization unless otherwise specified. All models are trained under comparable settings to isolate architectural effects. We first apply simple uniform n-bit per-channel quantization of weights, and then m-bit per-tensor quantization of activations, and denote it as WnAm. We report accuracy task-wise and averaged across tasks with more results in Section E.

Residual-free with KL Shampoo and temperature scaling performs the best. We first study the optimization behavior of residual-free transformers. In practice, we observe that residual-free transformers become increasingly difficult to train with AdamW as depth increases. We then evaluate several second-order optimizers, including SOAP, Muon, and KL Shampoo. As shown in Figure 3 (left), all optimizers enable trainability of residual-free models, which is consistent with the theory in Section 3.2. In addition, *KL Shampoo achieves the lowest training loss and SOAP is slightly worse, while Muon converges slowly.* We further find that *the depth-aware attention temperature scaling leads to lower training loss* (Figure 3 (middle)). This supports our hypothesis that controlling the sharpness of attention distributions is critical in deep residual-free networks, where repeated dense mixing can otherwise lead to signal attenuation or amplification. In the remainder of this section, we use KL Shampoo with temperature scaling as our default configuration for residual-free models.

Residual-free transformers yield near-Gaussian activations. We now compare the activation distribution of residual and residual-free transformers. For a fair comparison, we include residual

Table 1: **Residual-free transformers are substantially quantization robust.** Zero-shot performance (average accuracy) comparison across models under BF16, W8A12, W8A8, and W8A6.

Quant.	Model	arc_c	arc_e	boolq	hellaswag	openbookqa	piqa	social_iqa	winogrande	avg
BF16	Residual + AdamW	0.257	0.488	0.583	0.370	0.330	0.653	0.383	0.524	0.449
	Residual + KL Shampoo	0.265	0.513	0.582	0.385	0.312	0.650	0.396	0.514	0.452
	Residual-Free + KL Shampoo	0.257	0.463	0.606	0.343	0.316	0.616	0.371	0.511	0.435
W8A12	Residual + AdamW	0.232	0.334	0.500	0.295	0.264	0.526	0.347	0.521	0.378
	Residual + KL Shampoo	0.265	0.510	0.596	0.377	0.318	0.641	0.387	0.526	0.453
	Residual-Free + KL Shampoo	0.252	0.450	0.589	0.345	0.318	0.617	0.366	0.524	0.433
W8A8	Residual + AdamW	0.273	0.284	0.507	0.263	0.272	0.500	0.346	0.510	0.369
	Residual + KL Shampoo	0.222	0.401	0.578	0.311	0.270	0.565	0.349	0.521	0.402
	Residual-Free + KL Shampoo	0.247	0.448	0.590	0.344	0.292	0.611	0.370	0.529	0.429
W8A6	Residual + AdamW	0.279	0.262	0.619	0.263	0.272	0.503	0.326	0.515	0.380
	Residual + KL Shampoo	0.277	0.263	0.380	0.258	0.244	0.505	0.348	0.513	0.348
	Residual-Free + KL Shampoo	0.243	0.415	0.553	0.331	0.296	0.582	0.366	0.527	0.414

transformers trained with both AdamW and KL Shampoo. As shown in Figure 3 (right), residual transformers trained with AdamW exhibit rapidly increasing excess kurtosis, which continues to grow throughout training. This indicates that activations become increasingly heavy-tailed and deviate from Gaussianity. Training with KL Shampoo significantly reduces this growth, but excess kurtosis remains high, thus non-Gaussian activations. In contrast, *residual-free transformers trained with KL Shampoo maintain excess kurtosis close to zero across the entire training trajectory*, indicating that activations remain near-Gaussian. These results highlight that optimization alone can partially mitigate non-Gaussianity in residual models, but cannot eliminate it. Removing the residual connection allows dense mixing to consistently contract higher-order moments and stabilize activation distributions, consistent with our theory (Section 3.2). Figure 4 shows the activation distributions where the residual-free transformer exhibits a near-Gaussian distribution with excess kurtosis close to 0, whereas both residual models produce sharply peaked, heavy-tailed distributions with extreme outliers, even with KL Shampoo. This confirms that KL Shampoo mitigates but does not remove the non-Gaussian activation structure induced by residual architectures. More analyses across training are in Section E.

Residual-free transformers are substantially quantization robust. We next evaluate how these differences in activation distribution actually affect quantization. Table 1 shows, at full precision (BF16), the residual-free model incurs a small performance drop, and Residual + KL Shampoo slightly outperforms the others. As precision decreases, the gap between architectures becomes pronounced. The Residual + AdamW model degrades rapidly, with accuracy dropping from 0.449 at BF16 to 0.369 at W8A8 (−8%). This behavior is consistent with its heavy-tailed activation distributions, which introduce large quantization errors. Using KL Shampoo appears to improve robustness for residual models in reasonably high-bit quantization (W8A12). However, note that it degrades substantially from 0.452 to 0.348 when aggressively quantized to W8A6. Thus, it shows that KL Shampoo can reduce activation non-Gaussianity, though it does not eliminate it. In contrast, *the residual-free transformer is consistently the most robust across all low-precision settings*. While slightly weaker at BF16, it surpasses residual models under quantization, achieving higher average accuracy by +2.7% points at W8A8 and +6.6% points at W8A6. Notably, its performance degrades much more slowly as precision decreases, indicating that it is more compatible in this uniform low-bit quantization protocol. Additional results at a higher precision of W16 are provided in Section E.

6 Discussion and Conclusion

To the best of our knowledge, this work is the first to identify and study the quantization-relevant consequences of residual-free transformer architectures. Our central finding is that quantization difficulty is not only a property of the quantizer, but also of the activation distributions induced by the architecture. In particular, residual connections preserve and can amplify non-Gaussian activation statistics during training, producing heavy-tailed activations that are poorly matched to simple low-bit quantization. In contrast, when residual-free transformers are combined with orthogonal initialization and isometry-preserving optimization, their activations remain close to Gaussian across depth and training time. We deliberately evaluate this effect using simple uniform quantization. Modern quantization pipelines often include rotations, clipping, equivalent transformations, per-channel or per-token scaling, and mixed-precision outlier handling, all of which can compensate for, and therefore obscure, the architectural source of quantization error. Our goal is not to replace such

methods, but to isolate whether the transformer architecture itself produces quantization-unfriendly activation statistics. Under this diagnostic, residual-free transformers show substantially improved robustness to low-bit quantization, despite a modest full-precision performance gap.

More broadly, our results suggest that quantization robustness should be viewed not only as a post-training compression problem, but also as an architectural and optimization problem. Residual-free models close much of the trainability gap reported in prior work, extending from shallow regimes to moderately deep transformers, while producing activation statistics that are intrinsically more compressible. Important limitations remain, including the full-precision accuracy gap, scaling to greater depths and model sizes, and understanding how residual-free architectures interact with stronger quantization pipelines. Nevertheless, our findings provide a step toward quantization-friendly foundation models and suggest that future work should jointly consider architecture, optimization, and compression rather than treating them in isolation.

References

- S. Ashkboos, A. Mohtashami, M. L. Croci, B. Li, P. Cameron, M. Jaggi, D. Alistarh, T. Hoefler, and J. Hensman. QuaRot: Outlier-free 4-bit inference in rotated LLMs. *Advances in Neural Information Processing Systems*, 37:100213–100240, 2024.
- J. L. Ba, J. R. Kiros, and G. E. Hinton. Layer normalization. *arXiv preprint arXiv:1607.06450*, 2016.
- J. Bernstein, Y.-X. Wang, K. Azizzadenesheli, and A. Anandkumar. signSGD: Compressed optimisation for non-convex problems. In *International conference on machine learning*, pages 560–569. PMLR, 2018.
- Y. Bisk, R. Zellers, J. Gao, Y. Choi, et al. Piqa: Reasoning about physical commonsense in natural language. In *Proceedings of the AAAI conference on artificial intelligence*, volume 34, pages 7432–7439, 2020.
- Y. Bondarenko, M. Nagel, and T. Blankevoort. Understanding and overcoming the challenges of efficient transformer quantization. In *Proceedings of the 2021 Conference on Empirical Methods in Natural Language Processing*, pages 7947–7969, 2021.
- Y. Bondarenko, M. Nagel, and T. Blankevoort. Quantizable transformers: Removing outliers by helping attention heads do nothing. *Advances in Neural Information Processing Systems*, 36:75067–75096, 2023.
- C. Clark, K. Lee, M.-W. Chang, T. Kwiatkowski, M. Collins, and K. Toutanova. Boolq: Exploring the surprising difficulty of natural yes/no questions. In *Proceedings of the 2019 conference of the north American chapter of the association for computational linguistics: Human language technologies, volume 1 (long and short papers)*, pages 2924–2936, 2019.
- P. Clark, I. Cowhey, O. Etzioni, T. Khot, A. Sabharwal, C. Schoenick, and O. Tafjord. Think you have solved question answering? try arc, the ai2 reasoning challenge. *arXiv preprint arXiv:1803.05457*, 2018.
- T. Dao. FlashAttention-2: Faster attention with better parallelism and work partitioning. In *International Conference on Learning Representations (ICLR)*, 2024.
- T. Dao, D. Y. Fu, S. Ermon, A. Rudra, and C. Ré. FlashAttention: Fast and memory-efficient exact attention with IO-awareness. In *Advances in Neural Information Processing Systems (NeurIPS)*, 2022.
- T. Dettmers, M. Lewis, Y. Belkada, and L. Zettlemoyer. Gpt3. int8 (): 8-bit matrix multiplication for transformers at scale. *Advances in neural information processing systems*, 35:30318–30332, 2022.
- T. Dettmers, A. Pagnoni, A. Holtzman, and L. Zettlemoyer. Qlora: Efficient finetuning of quantized llms. *Advances in neural information processing systems*, 36:10088–10115, 2023.
- X. Glorot and Y. Bengio. Understanding the difficulty of training deep feedforward neural networks. In *Proceedings of the thirteenth international conference on artificial intelligence and statistics*, pages 249–256. JMLR Workshop and Conference Proceedings, 2010.
- V. Gupta, T. Koren, and Y. Singer. Shampoo: Preconditioned stochastic tensor optimization. In *International Conference on Machine Learning*, pages 1842–1850. PMLR, 2018.
- M. Hardt and T. Ma. Identity matters in deep learning. In *International Conference on Learning Representations*, 2017.
- B. He, J. Martens, G. Zhang, A. Botev, A. Brock, S. L. Smith, and Y. W. Teh. Deep transformers without shortcuts: Modifying self-attention for faithful signal propagation. In *The Eleventh International Conference on Learning Representations*, 2023.
- B. He, L. Noci, D. Paliotta, I. Schlag, and T. Hofmann. Understanding and minimising outlier features in transformer training. In *Advances in Neural Information Processing Systems*, 2024.
- K. He, X. Zhang, S. Ren, and J. Sun. Delving deep into rectifiers: Surpassing human-level performance on imagenet classification. In *Proceedings of the IEEE international conference on computer vision*, pages 1026–1034, 2015.
- K. He, X. Zhang, S. Ren, and J. Sun. Deep residual learning for image recognition. In *Proceedings of the IEEE conference on computer vision and pattern recognition*, pages 770–778, 2016.
- J. Hoffmann, S. Borgeaud, A. Mensch, E. Buchatskaya, T. Cai, E. Rutherford, D. Casas, L. A. Hendricks, J. Welbl, A. Clark, et al. Training compute-optimal large language models. *arXiv preprint arXiv:2203.15556*, 10, 2022.

- Y. Huang, Y. Cheng, A. Bapna, O. Firat, D. Chen, M. Chen, H. Lee, J. Ngiam, Q. V. Le, Y. Wu, et al. Gpipe: Efficient training of giant neural networks using pipeline parallelism. *Advances in neural information processing systems*, 32, 2019.
- Y. Ji, J. Martens, J. Zheng, Z. Zhou, P. Moghadam, X. Zhang, H. Saratchandran, and S. Lucey. Cutting the skip: Training residual-free transformers. In *The Fourteenth International Conference on Learning Representations*, 2026.
- K. Jordan, Y. Jin, V. Boza, J. You, F. Cesista, L. Newhouse, and J. Bernstein. Muon: An optimizer for hidden layers in neural networks. Online manuscript, 2024.
- D. P. Kingma and J. Ba. Adam: A method for stochastic optimization. In *International Conference on Learning Representations*, 2015.
- Y. Li, X. Dong, and W. Wang. Additive powers-of-two quantization: An efficient non-uniform discretization for neural networks. In *International Conference on Learning Representations*, 2020.
- W. Lin, S. C. Lowe, F. Dangel, R. Eschenhagen, Z. Xu, and R. B. Grosse. Understanding and improving shampoo and soap via kullback-leibler minimization. *arXiv preprint arXiv:2509.03378*, 2025.
- Z. Liu, C. Zhao, I. Fedorov, B. Soran, D. Choudhary, R. Krishnamoorthi, V. Chandra, Y. Tian, and T. Blankevoort. SpinQuant: LLM quantization with learned rotations. In *International Conference on Learning Representations*, 2025.
- I. Loshchilov and F. Hutter. Decoupled weight decay regularization. In *International Conference on Learning Representations*, 2019.
- J. Martens, A. Ballard, G. Desjardins, G. Swirszcz, V. Dalibard, J. Sohl-Dickstein, and S. S. Schoenholz. Rapid training of deep neural networks without skip connections or normalization layers using deep kernel shaping. *arXiv preprint arXiv:2110.01765*, 2021.
- P. Micikevicius, D. Stosic, N. Burgess, M. Cornea, P. Dubey, R. Grisenthwaite, S. Ha, A. Heinecke, P. Judd, J. Kamalu, et al. FP8 formats for deep learning. *arXiv preprint arXiv:2209.05433*, 2022.
- T. Mihaylov, P. Clark, T. Khot, and A. Sabharwal. Can a suit of armor conduct electricity? a new dataset for open book question answering. In *Proceedings of the 2018 conference on empirical methods in natural language processing*, pages 2381–2391, 2018.
- D. Narayanan, A. Harlap, A. Phanishayee, V. Seshadri, N. R. Devanur, G. R. Ganger, P. B. Gibbons, and M. Zaharia. Pipedream: Generalized pipeline parallelism for dnn training. In *Proceedings of the 27th ACM symposium on operating systems principles*, pages 1–15, 2019.
- A. Nrusimha, M. Mishra, N. Wang, D. Alistarh, R. Panda, and Y. Kim. Mitigating the impact of outlier channels for language model quantization with activation regularization. *arXiv preprint arXiv:2404.03605*, 2024.
- K. Pearson. “das fehlergesetz und seine verallgemeinerungen durch fechner und pearson.” a rejoinder. *Biometrika*, 4(1-2):169–212, 1905.
- G. Penedo, H. Kydlíček, A. Lozhkov, M. Mitchell, C. Raffel, L. Von Werra, T. Wolf, et al. The fineweb datasets: Decanting the web for the finest text data at scale. *Advances in Neural Information Processing Systems*, 37: 30811–30849, 2024.
- J. Pennington, S. Schoenholz, and S. Ganguli. Resurrecting the sigmoid in deep learning through dynamical isometry: theory and practice. *Advances in neural information processing systems*, 30, 2017.
- S. Rajbhandari, J. Rasley, O. Ruwase, and Y. He. Zero: Memory optimizations toward training trillion parameter models. In *SC20: international conference for high performance computing, networking, storage and analysis*, pages 1–16. IEEE, 2020.
- K. Sakaguchi, R. L. Bras, C. Bhagavatula, and Y. Choi. Winogrande: An adversarial winograd schema challenge at scale. *Communications of the ACM*, 64(9):99–106, 2021.
- M. Sap, H. Rashkin, D. Chen, R. Le Bras, and Y. Choi. Social iqa: Commonsense reasoning about social interactions. In *Proceedings of the 2019 conference on empirical methods in natural language processing and the 9th international joint conference on natural language processing (EMNLP-IJCNLP)*, pages 4463–4473, 2019.
- A. Saxe, J. McClelland, and S. Ganguli. Exact solutions to the nonlinear dynamics of learning in deep linear neural networks. In *Proceedings of the International Conference on Learning Representations 2014*. International Conference on Learning Representations 2014, 2014.

- S. S. Schoenholz, J. Gilmer, S. Ganguli, and J. Sohl-Dickstein. Deep information propagation. In *International Conference on Learning Representations*, 2017.
- M. Shoeybi, M. Patwary, R. Puri, P. LeGresley, J. Casper, and B. Catanzaro. Megatron-lm: Training multi-billion parameter language models using model parallelism. *arXiv preprint arXiv:1909.08053*, 2019.
- R. K. Srivastava, K. Greff, and J. Schmidhuber. Training very deep networks. *Advances in neural information processing systems*, 28, 2015.
- N. Vyas, D. Morwani, R. Zhao, I. Shapira, D. Brandfonbrener, L. Janson, and S. M. Kakade. SOAP: Improving and stabilizing shampoo using adam for language modeling. In *The Thirteenth International Conference on Learning Representations*, 2025.
- X. Wei, Y. Zhang, X. Zhang, R. Gong, S. Zhang, Q. Zhang, F. Yu, and X. Liu. Outlier suppression: Pushing the limit of low-bit transformer language models. *Advances in Neural Information Processing Systems*, 35: 17402–17414, 2022.
- X. Wei, Y. Zhang, Y. Li, X. Zhang, R. Gong, J. Guo, and X. Liu. Outlier suppression+: Accurate quantization of large language models by equivalent and effective shifting and scaling. In *Proceedings of the 2023 Conference on Empirical Methods in Natural Language Processing*, pages 1648–1665, 2023.
- G. Xiao, J. Lin, M. Seznec, H. Wu, J. Demouth, and S. Han. Smoothquant: Accurate and efficient post-training quantization for large language models. In *International conference on machine learning*, pages 38087–38099. PMLR, 2023.
- L. Xiao, Y. Bahri, J. Sohl-Dickstein, S. Schoenholz, and J. Pennington. Dynamical isometry and a mean field theory of CNNs: How to train 10,000-layer vanilla convolutional neural networks. In *International conference on machine learning*, pages 5393–5402. PMLR, 2018.
- R. Xiong, Y. Yang, D. He, K. Zheng, S. Zheng, C. Xing, H. Zhang, Y. Lan, L. Wang, and T. Liu. On layer normalization in the transformer architecture. In *International conference on machine learning*, pages 10524–10533. PMLR, 2020.
- Y. Xu, H. Lee, D. Chen, B. Hechtman, Y. Huang, R. Joshi, M. Krikun, D. Lepikhin, A. Ly, M. Maggioni, et al. GSPMD: general and scalable parallelization for ml computation graphs. *arXiv preprint arXiv:2105.04663*, 2021.
- S. Zagoruyko and N. Komodakis. DiracNets: Training very deep neural networks without skip-connections. *arXiv preprint arXiv:1706.00388*, 2017.
- A. Zandieh, M. Daliri, M. Hadian, and V. Mirrokni. Turboquant: Online vector quantization with near-optimal distortion rate. *arXiv preprint arXiv:2504.19874*, 2025.
- R. Zellers, A. Holtzman, Y. Bisk, A. Farhadi, and Y. Choi. Hellaswag: Can a machine really finish your sentence? In *Proceedings of the 57th annual meeting of the association for computational linguistics*, pages 4791–4800, 2019.
- B. Zhang and R. Sennrich. Root mean square layer normalization. *Advances in neural information processing systems*, 32, 2019.

Supplementary Material

Contents

1	Introduction	1
2	Related Work	3
3	Analysis of Activations of Residual and Residual-Free Transformers	3
3.1	Setup and Preliminaries	3
3.2	Theoretical Analysis of Layerwise Activation Distributions	4
4	Practical Recipe to Train Deep Residual-Free Transformers	7
5	Experimental Results	8
6	Discussion and Conclusion	9
A	Related Work	15
B	Preliminary Definitions	16
B.1	Notations	16
B.2	Residual and Residual-Free blocks in Transformers	16
B.3	Initializations	16
B.4	Optimizers	17
C	Analysis of Layer-Wise Activations of Residual and Residual-Free Transformers	17
C.1	Normalization is Necessary to Control Variance	17
C.2	Auxiliary Lemmas on Excess Kurtosis	18
C.3	Excess Kurtosis Behavior of Different Initializations: Orthogonal vs Gaussian	20
C.4	Excess Kurtosis Behavior of Optimizers: Spectral GD vs Sign GD	20
C.5	Excess Kurtosis Behavior in Residual Settings	22
C.6	When Residual-Free Can Remain Near-Gaussian While Residual Transformer Need Not	23
D	Experimental Details	27
E	Additional Experiments	28
E.1	Residual-free Transformers With Second-Order Optimizations	28
E.2	Residual and Residual-Free Transformers: Activation Distribution	29
E.3	Residual and Residual-Free Transformers: W8 Quantization Results	32
E.4	Residual and Residual-Free Transformers: W16 Quantization Results	33
E.5	Residual and Residual-Free Transformers: Weight Full Precision Quantization Results	35
F	Broader Impact Statement	37

A Related Work

Residual-free transformers. Prior work [He et al., 2023] has investigated training transformers without residual connections or normalization by modifying the self-attention block. Based on their observation that residual-free transformers suffer from rank collapse, where the kernel matrix converges in depth to have rank 1, they modified the Self-Attention Block to maintain well-behaved kernels at initialization. However, their techniques require 5 times more training steps to achieve a comparable training loss than the residual-based methods. Further, Ji et al. [2026] showed that residual-free transformers can be trained as efficiently as their residual-based counterparts through a principled initialization of the self-attention block alone, without any architectural modification. Their approach is also hardware-friendly and remains compatible with optimizations such as Flash Attention Dao et al. [2022], Dao [2024]. They demonstrated the benefits of residual-free architectures in the vision domain, where learned features are more abstract and semantically consistent. However, their method still struggles to scale to deeper networks, for example, beyond 12 layers.

Training deep networks without residuals. The challenge of training very deep networks without explicit skip connections predates transformers. Highway networks and residual networks were introduced to address optimization difficulties in depth [Srivastava et al., 2015, He et al., 2016]. Other approaches attempt to recover trainability through parameterization or initialization, including identity and Dirac parameterizations [Hardt and Ma, 2017, Zagoruyko and Komodakis, 2017], orthogonal initialization and dynamical-isometry analyses [Saxe et al., 2014, Pennington et al., 2017, Schoenholz et al., 2017, Xiao et al., 2018]. These works primarily focus on optimization, signal propagation, or representation learning. Our focus is different and we ask how the presence or absence of residual paths affects activation distributions and their suitability for low-bit quantization.

Activation outliers and transformer quantization. A large body of work has shown that transformer quantization is often limited by activation outliers and high dynamic range rather than by weights alone. LLM.int8() identifies systematic emergent outlier features in large language models and handles them through mixed-precision decomposition [Dettmers et al., 2022]. SmoothQuant observes that activations are harder to quantize than weights and migrates activation outlier difficulty into weights through an equivalent transformation [Xiao et al., 2023]. Outlier Suppression and Outlier Suppression+ mitigate activation outliers through shifting and scaling transformations [Wei et al., 2022, 2023]. Bondarenko et al. [2021] show that transformer activations have high dynamic range and structured outliers that make low-bit fixed-point quantization difficult. Bondarenko et al. [2023] further connect strong activation outliers to attention heads that learn no-op or partial updates in the residual stream. He et al. [2024] study outlier features during transformer training and show that architectural and optimization choices affect their emergence, using metrics including kurtosis over activation norms. Nrusimha et al. [2024] show that outlier channels emerge early in language model training, occur more frequently in layers with residual streams, and can be mitigated through activation regularization. These works motivate our focus on architectural sources of quantization difficulty. Our contribution is to isolate, in controlled residual versus residual-free comparisons, how residual addition affects activation Gaussianity and quantization error.

Rotation and outlier-removal methods. Recent quantization methods also reduce activation outliers by exploiting rotational invariances. QuaRot applies orthogonal rotations to hidden states, feedforward activations, attention components, and the KV cache to obtain outlier-free 4-bit inference without changing the full-precision function [Ashkboos et al., 2024]. SpinQuant learns such rotations to improve quantized accuracy beyond random rotations [Liu et al., 2025]. TurboQuant similarly uses randomized rotations and vector quantization to reduce outlier-induced distortion in low-bit compression [Zandieh et al., 2025]. These methods are closely related in spirit to our use of dense orthogonal mixing: all suggest that distributing information across coordinates can make activations easier to quantize. The distinction is that rotation-based methods modify or transform a trained residual model for quantization, whereas our work studies whether quantization-friendly activation statistics can be encouraged during training through residual-free architecture, orthogonal initialization, and isometry-preserving optimization.

Positioning of our work. Overall, prior work has established that activation outliers are a central obstacle for transformer quantization and has proposed increasingly effective methods to compensate for them after or during training. In contrast, we study a source-level architectural problem and understand the mechanism that results in non-Gaussian activations in the first place.

B Preliminary Definitions

B.1 Notations

We denote vectors and matrices using boldface notation. Specifically, bold lowercase letters such as \mathbf{v} denote vectors, and bold uppercase letters such as \mathbf{M} denote matrices. For a vector $\mathbf{v} \in \mathbb{R}^d$, we denote its i -th coordinate by v_i . For a matrix $\mathbf{M} \in \mathbb{R}^{m \times n}$, we denote its (i, j) -th entry by M_{ij} . We use $\|\cdot\|$ to denote the Euclidean norm for vectors and the spectral norm for matrices unless otherwise specified. The identity matrix of dimension d is denoted by \mathbf{I}_d . For a function f , we use ∇f to denote its gradient. Throughout the paper, we consider sequences of representations $\{\mathbf{X}_\ell\}_{\ell=0}^L$, where ℓ indexes the layer of the network.

B.2 Residual and Residual-Free blocks in Transformers

We write out the definitions of residual and residual-free blocks in Section 3 for completion. Let $\mathbf{X}_\ell \in \mathbb{R}^{T \times d}$ denote the token representation at layer ℓ , where T is the sequence length and d is the model dimension. Each transformer block consists of a self-attention map $\text{SA}(\cdot)$ and a position-wise feedforward map $\text{MLP}(\cdot)$, both applied to normalized inputs through $\text{norm}(\cdot)$. For a residual transformer,

$$\begin{aligned} \mathbf{Y}_\ell &= \mathbf{X}_{\ell-1} + \text{SA}(\text{norm}(\mathbf{X}_{\ell-1})), \\ \mathbf{X}_\ell &= \mathbf{Y}_\ell + \text{MLP}(\text{norm}(\mathbf{Y}_\ell)). \end{aligned} \quad (7)$$

The residual-free counterpart removes the additive skip paths,

$$\begin{aligned} \mathbf{Y}_\ell &= \text{SA}(\text{norm}(\mathbf{X}_{\ell-1})), \\ \mathbf{X}_\ell &= \text{MLP}(\text{norm}(\mathbf{Y}_\ell)). \end{aligned} \quad (8)$$

This distinction, the presence or absence of the additive identity path, is the architectural feature we isolate in the analysis. Here $\text{norm}(\cdot)$ denotes either layer normalization Ba et al. [2016] or RMS normalization [Zhang and Sennrich, 2019], and serves to control the scale of the input to each sublayer. The self-attention operation $\text{SA}(\cdot)$ for any input \mathbf{X} is defined as

$$\text{SA}(\mathbf{X}) = \mathbf{A}\mathbf{V}\mathbf{W}^O,$$

where $\mathbf{Q} = \mathbf{X}\mathbf{W}^Q$, $\mathbf{K} = \mathbf{X}\mathbf{W}^K$, $\mathbf{V} = \mathbf{X}\mathbf{W}^V$, and the attention matrix is $\mathbf{A} = \text{softmax}(\frac{1}{\sqrt{d}}\mathbf{Q}\mathbf{K}^T)$. The parameter matrices $\mathbf{W}^Q, \mathbf{W}^K, \mathbf{W}^V, \mathbf{W}^O \in \mathbb{R}^{d \times d}$ are learnable. In practice, $\text{SA}(\cdot)$ is multi-head attention with h heads and has the form

$$\text{SA}(\mathbf{X}) = \text{Concat}(\mathbf{A}_1\mathbf{V}_1, \dots, \mathbf{A}_h\mathbf{V}_h)\mathbf{W}^O,$$

where \mathbf{A}_i are attention matrices with projection matrices $\mathbf{W}_i^Q, \mathbf{W}_i^K, \mathbf{W}_i^V \in \mathbb{R}^{d \times d_h}$, $d_h = \frac{d}{h}$ and \mathbf{W}^O is the output projection. The MLP block has the form

$$\text{MLP}(\mathbf{X}) = \phi(\mathbf{X}\mathbf{W}^U)\mathbf{W}^D,$$

where ϕ is a pointwise nonlinearity such as GELU, and $\mathbf{W}^U \in \mathbb{R}^{d \times d_f}$ and $\mathbf{W}^D \in \mathbb{R}^{d_f \times d}$ are the up-projection and down-projection learnable matrices, respectively, d_f is the hidden dimension (typically $d_f = 4d$). Thus, at the level of a single coordinate or token, each sublayer repeatedly applies a nonlinear transformation and mixes coordinates through matrices such as \mathbf{W}^O and \mathbf{W}^D .

B.3 Initializations

Gaussian initialization. In standard deep learning frameworks such as PyTorch, linear layers are typically initialized using variance-preserving schemes such as Xavier (Glorot) [Glorot and Bengio, 2010] or Kaiming [He et al., 2015] initializations. For example, for a weight matrix $\mathbf{W} \in \mathbb{R}^{m \times n}$, Xavier initialization samples $W_{ij} \sim \mathcal{N}\left(0, \frac{2}{m+n}\right)$, while Kaiming initialization (for ReLU activations) uses $W_{ij} \sim \mathcal{N}\left(0, \frac{2}{n}\right)$. These schemes aim to preserve the variance of activations across layers at initialization.

Orthogonal initialization. The weight matrix $\mathbf{W} \in \mathbb{R}^{d \times d}$ is initialized such that $\mathbf{W}\mathbf{W}^\top = \mathbf{I}_d$ [Saxe et al., 2014]. For rectangular matrices, one constructs a semi-orthogonal matrix whose columns (or rows) are orthonormal. Often, a scaling factor is applied: $\mathbf{W} = \alpha \tilde{\mathbf{W}}$, $\tilde{\mathbf{W}}^\top \tilde{\mathbf{W}} = \mathbf{I}$, where α controls the variance of activations. Orthogonal initialization preserves norms and helps maintain dynamical isometry, which is beneficial for training very deep networks.

B.4 Optimizers

Sign gradient descent. Sign gradient descent is a simplified optimization method that updates parameters using only the sign of the gradient [Bernstein et al., 2018]. It serves as a useful proxy for adaptive methods such as Adam [Kingma and Ba, 2015], AdamW [Loshchilov and Hutter, 2019]. Given parameters \mathbf{W} and loss $\mathcal{L}(\mathbf{W})$, the update rule is

$$\mathbf{W}_{t+1} = \mathbf{W}_t - \eta \text{sign}(\nabla \mathcal{L}(\mathbf{W}_t)), \quad (9)$$

where $\eta > 0$ is the learning rate and the sign function is applied elementwise. This method captures the directionality of adaptive optimizers while discarding magnitude information.

Spectral gradient descent. Spectral gradient descent is a simplified model of modern second-order optimization methods such as Shampoo [Gupta et al., 2018], Muon [Jordan et al., 2024], SOAP [Vyas et al., 2025], and KL-Shampoo [Lin et al., 2025]. These methods precondition the gradient using curvature information. Let $\mathbf{W} \in \mathbb{R}^{m \times n}$ be a weight matrix with gradient $\mathbf{G} = \nabla \mathcal{L}(\mathbf{W})$. A generic spectral gradient descent updates \mathbf{W} as

$$\mathbf{W}_{t+1} = \mathbf{W}_t - \eta \mathbf{P}_t^{-1/4} \mathbf{G}_t \mathbf{Q}_t^{-1/4},$$

where $\mathbf{P}_t, \mathbf{Q}_t$ are positive definite preconditioning matrices. In matrix form, a common approximation is $\mathbf{P}_t = \mathbf{G}_t \mathbf{G}_t^\top$ and $\mathbf{Q}_t = \mathbf{G}_t^\top \mathbf{G}_t$. Considering the eigenvalue decomposition of $\mathbf{G}_t = \mathbf{U}\mathbf{S}\mathbf{V}^\top$, thus $\mathbf{G}_t \mathbf{G}_t^\top = \mathbf{U}\mathbf{S}^2\mathbf{U}^\top$ and $\mathbf{G}_t^\top \mathbf{G}_t = \mathbf{V}\mathbf{S}^2\mathbf{V}^\top$ hence the update is

$$\begin{aligned} \mathbf{W}_{t+1} &= \mathbf{W}_t - \eta \mathbf{U}\mathbf{S}^{-1/2}\mathbf{S}\mathbf{S}^{-1/2}\mathbf{V}^\top \\ &= \mathbf{W}_t - \eta \mathbf{U}\mathbf{V}^\top \end{aligned} \quad (10)$$

This effectively rescales updates along different eigendirections, normalizing by curvature. Spectral gradient descent captures the key behavior of matrix-preconditioned optimizers while remaining analytically tractable. In particular, it preserves invariances under linear reparameterizations and tends to equalize progress across different directions in parameter space.

C Analysis of Layer-Wise Activations of Residual and Residual-Free Transformers

We start with analyzing the need for normalization $\text{norm}(\cdot)$ as it controls the second moments in both residual and residual-free transformers.

C.1 Normalization is Necessary to Control Variance

We consider the layerwise recursions defined in Section B.2 and analyze the behavior of the variance across layers. We expand and include further technical details to Lemma 1 as follows:

Lemma 5 (Normalization controls variance collapse and growth). *Consider the residual and residual-free update in Eqs. (1) and (2) without normalization, that is, $\text{norm}(\mathbf{X}) = \mathbf{X}$. Assume coordinates of \mathbf{X}_ℓ are centered with variance q_ℓ , and weight matrices are variance-preserving. Then,*

- **Residual-free case:** The variance of $\mathbf{X}_{\ell+1}$, $q_{\ell+1} \approx \mathbb{E}_{z \sim \mathcal{N}(0, q_\ell)}[\phi(z)^2]$, which yields $q_{\ell+1} = cq_\ell$ with $c < 1$ for common nonlinearities that contracts the input. Hence, the variance of deep layers $q_L \rightarrow 0$ exponentially with depth.
- **Residual case:** The variance of $\mathbf{X}_{\ell+1}$, $q_{\ell+1} \approx (1 + c)q_\ell$ with $c > 0$ under weak correlation, so q_L grows exponentially with depth.

Proof of Lemma 5. We give the proof for a single normalized-width sublayer, since the same argument applies to both the attention output projection and the MLP projection under the variance-preserving approximation. Write the sublayer as

$$F_\ell(\mathbf{X}_\ell) = \mathbf{W}_\ell \phi(\mathbf{X}_\ell),$$

where \mathbf{W}_ℓ is independent of \mathbf{X}_ℓ and variance-preserving. For a single coordinate, this means

$$\mathbb{E}[(F_\ell(\mathbf{X}_\ell))_i^2 \mid \phi(\mathbf{X}_\ell)] = \frac{1}{d} \sum_{j=1}^d \phi(X_{\ell,j})^2.$$

Taking expectation gives

$$\text{Var}((F_\ell(\mathbf{X}_\ell))_i) \approx \mathbb{E}_{z \sim \mathcal{N}(0, q_\ell)}[\phi(z)^2].$$

Thus, if the coordinates of \mathbf{X}_ℓ are centered with variance q_ℓ , the residual-free recursion satisfies

$$q_{\ell+1} \approx \mathbb{E}_{z \sim \mathcal{N}(0, q_\ell)}[\phi(z)^2].$$

For common pointwise nonlinearities such as ReLU and GELU, and vectorwise linearities like softmax, the variance contracts as these functions contract the input value. Therefore,

$$q_{\ell+1} = cq_\ell,$$

where $c < 1$. Therefore, by induction,

$$q_\ell = c^\ell q_0.$$

Exemplary, in the case of ReLU, $c = \frac{1}{2}$, which can be derived using the symmetry of the Gaussian. Hence, without normalization or gain correction, the variance of a residual-free network collapses exponentially with depth. For the residual recursion,

$$\mathbf{X}_{\ell+1} = \mathbf{X}_\ell + F_\ell(\mathbf{X}_\ell).$$

For one coordinate,

$$\begin{aligned} q_{\ell+1} &= \text{Var}(X_{\ell i} + F_{\ell i}) = \text{Var}(X_{\ell i}) + \text{Var}(F_{\ell i}) + 2 \text{Cov}(X_{\ell i}, F_{\ell i}) \\ &= q_\ell + \text{Var}(F_{\ell, i}) + 2 \text{Cov}(X_{\ell, i}, F_{\ell, i}) \end{aligned}$$

Under the standard mean-field approximation that the residual branch is weakly correlated with the input coordinate, the covariance term is negligible, giving

$$q_{\ell+1} \approx q_\ell + \mathbb{E}_{z \sim \mathcal{N}(0, q_\ell)}[\phi(z)^2] = (1 + c)q_\ell.$$

Hence, in this case, the variance grows exponentially with depth. \square

Remark 1. *Layer normalization prevents both effects by re-centering and rescaling the input to each sublayer, whereas RMSNorm only rescales the input to each sublayer. Both ensure that the variance of the inputs to SA(\cdot) and MLP(\cdot) remains $\mathcal{O}(1)$ across layers.*

C.2 Auxiliary Lemmas on Excess Kurtosis

We now introduce the excess kurtosis Definition 1, which is a scalar proxy for deviation from Gaussianity [Pearson, 1905]. Excess kurtosis does not characterize a distribution completely, but it is a natural and tractable summary statistic for tail-heaviness and departure from Gaussian fourth moments. Notice that the input to each layer SA(\cdot) or MLP(\cdot) is normalized using norm(\cdot) which keep the variance controlled and $\mathcal{O}(1)$.

Definition 2 (Excess Kurtosis). *Let v be a random variable with $\mathbb{E}[v] = \mu$ and variance $\mathbb{E}[(v - \mu)^2] = \sigma^2$. Its excess kurtosis is defined as*

$$\gamma_v = \frac{\mathbb{E}[(v - \mu)^4]}{(\mathbb{E}[(v - \mu)^2])^2} - 3.$$

For a standardized random variable v , excess kurtosis is $\gamma_v = \mathbb{E}[v^4] - 3$. A standard Gaussian random variable has excess kurtosis equal to 0. Thus, values of γ_v close to 0 indicate that v is close to Gaussian in the fourth-moment sense.

We first record several elementary facts about the propagation of excess kurtosis through linear combinations. These lemmas will be used repeatedly in the later analysis.

Lemma 6 (Excess kurtosis of isotropic variance mixing). *Let $y = \sum_{i=1}^d a_i u_i$ where $u \in \mathbb{R}^d$ has independent coordinates and each random variable u_i is centered and has isotropic variance, that is, $\mathbb{E}[u_i] = 0$ and $\mathbb{E}[u_i^2] = 1$, and $a \in \mathbb{R}^d$ is a deterministic vector with unit norm $\sum_{i=1}^d a_i^2 = 1$. Assume further that for each u_i has the same excess kurtosis γ_u . Then excess kurtosis of y , γ_y is*

$$\gamma_y = \gamma_u \sum_{i=1}^d a_i^4.$$

Proof. The mean of y is $\sum_{i=1}^d a_i \mathbb{E}[u_i] = 0$ and the variance of y is $\sum_{i=1}^d a_i^2 \mathbb{E}[u_i^2] = \sum_{i=1}^d a_i^2 = 1$. Therefore, excess kurtosis of y is

$$\begin{aligned} \gamma_y &= \mathbb{E} \left[\left(\sum_{i=1}^d a_i u_i \right)^4 \right] - 3 \\ &= \mathbb{E} \left[\sum_{i=1}^d a_i^4 u_i^4 + 4 \sum_{i \neq j} a_i^3 u_i^3 a_j u_j + 6 \sum_{i \neq j} a_i^2 u_i^2 a_j^2 u_j^2 + 12 \sum_{i \neq j \neq k} a_i^2 u_i^2 a_j u_j a_k u_k + \right. \\ &\quad \left. 24 \sum_{i \neq j \neq k \neq l} a_i u_i a_j u_j a_k u_k a_l u_l \right] - 3 \\ &= \mathbb{E} \left[\sum_{i=1}^d a_i^4 u_i^4 + 6 \sum_{i \neq j} a_i^2 u_i^2 a_j^2 u_j^2 \right] - 3 \\ &= (\gamma_u + 3) \sum_{i=1}^d a_i^4 + 6 \sum_{i \neq j} a_i^2 a_j^2 - 3 \quad ; \gamma_u = \mathbb{E}[u_i^4] - 3, \mathbb{E}[u_i^2] = 1 \quad \forall i \end{aligned} \quad (11)$$

Since $\sum_{i=1}^d a_i^2 = 1$, squaring it will give

$$\begin{aligned} \left(\sum_{i=1}^d a_i^2 \right)^2 &= \sum_{i=1}^d a_i^4 + 2 \sum_{i \neq j} a_i^2 a_j^2 = 1 \\ 2 \sum_{i \neq j} a_i^2 a_j^2 &= 1 - \sum_{i=1}^d a_i^4 \end{aligned} \quad (12)$$

Substituting Eq. (12) in Eq. (11), we obtain

$$\begin{aligned} \gamma_y &= (\gamma_u + 3) \sum_{i=1}^d a_i^4 + 3 \left(1 - \sum_{i=1}^d a_i^4 \right) - 3 \\ &= \gamma_u \sum_{i=1}^d a_i^4 \end{aligned} \quad (13)$$

Thus proving the lemma. \square

Lemma 7 (Dense mixing implies $1/d$ excess kurtosis shrinkage). *Consider the setting of Lemma 6. Assume in addition that a is dense, then*

$$\gamma_y = \frac{\gamma_u}{d}.$$

Proof. When a is dense unit norm, it means $\sum_{i=1}^d a_i^2 = 1$ with the scale of a_i is roughly $\frac{1}{\sqrt{d}}$ for all i . Therefore,

$$\sum_{i=1}^d a_i^4 = \frac{1}{d}.$$

The claim then follows immediately from Eq. (13) as $\gamma_y = \frac{\gamma_u}{d}$. Thus, if u is non-Gaussian, then dense mixing suppresses it. \square

C.3 Excess Kurtosis Behavior of Different Initializations: Orthogonal vs Gaussian

Excess kurtosis behavior of orthogonal initialization. In Lemmas 6 and 7, orthogonality guarantees unit norm, that is $\sum_{i=1}^d a_i^2 = 1$. The conclusion of Lemma 7 does not hold for an arbitrary orthogonal a without the additional dense condition. To obtain $\sum_i a_i^4 = O(1/d)$, one needs a to be dense or incoherent, for example when $\max_i |a_i| \lesssim d^{-1/2}$. The case above gives the cleanest exact statement and captures the regime relevant for **dense orthogonal initializations**.

Corollary 1 (Near-Gaussianity after dense orthogonal mixing). *Under the assumptions of Lemma 7, $\gamma_y = \frac{\gamma_u}{d}$. In particular, y is close to Gaussian in the fourth-moment sense whenever $\gamma_u \ll d$. Equivalently, as $d \rightarrow \infty$, if $\gamma_u = o(d)$, then $\gamma_y \rightarrow 0$.*

Proof. y is close to Gaussian in the fourth-moment sense when its excess kurtosis γ_y is close to zero. It is straightforward to see that γ_y is close to 0 only if γ_u is much smaller than d . The asymptotic statement follows immediately. \square

Excess kurtosis behavior of default Gaussian initialization. A natural alternative to dense orthogonal mixing is default Gaussian initialization, for example, $a_i \sim \mathcal{N}(0, 1/d)$. This also produces dense rows with high probability, and one might therefore expect a similar $1/d$ excess kurtosis shrinkage. Indeed, a Gaussian row is dense in the sense that

$$\sum_{i=1}^d a_i^4 = \frac{3}{d}.$$

For a row normalized to unit norm, $a/\|a\|$ is approximately uniform on the sphere, and $\mathbb{E} \sum_i (a_i/\|a\|)^4 = 3/(d+2)$. Thus Gaussian rows are dense up to constants, and still yield $O(1/d)$ kurtosis shrinkage. The constant differs from the ideal equal-magnitude row. However, default Gaussian initialization is weaker than dense orthogonal initialization in two important ways. First, the row norm $\sum_{i=1}^d a_i^2$ is random for each row i , rather than exactly equal to one. Consequently, even if the input u is Gaussian, the output is a scale mixture of Gaussians over different rows, producing an additional finite-width excess kurtosis term of order $1/d$. For example, if u_i are independent standardized Gaussians and $a_i \sim \mathcal{N}(0, 1/d)$, then

$$\gamma_y = \frac{6}{d},$$

whereas a dense unit-norm (orthogonal) row gives $\gamma_y = 0$ for Gaussian inputs.

Second, and more importantly for deep networks, a Gaussian matrix preserves norms only in **expectation**. Its singular values are spread, so repeated composition can create anisotropic amplification and contraction across layers. Orthogonal initialization instead gives exact norm preservation at the linear level, and therefore avoids injecting layerwise variance disorder. Thus Gaussian initialization is a plausible candidate for one-layer kurtosis shrinkage, but dense orthogonal initialization provides stronger per-layer geometric control, which is crucial in deep compositions, attention blocks, and during training.

C.4 Excess Kurtosis Behavior of Optimizers: Spectral GD vs Sign GD

The key point in the excess kurtosis analysis is that dense approximately orthogonal mixing shrinks excess kurtosis and makes the activations more Gaussian. In this section, we analyze the excess kurtosis behavior of different optimizers from this standpoint. Spectral updates tend to maintain orthogonal mixing, whereas sign-like updates can destroy it much more rapidly. Once this dense near-isometric structure is lost, the excess kurtosis shrinkage from Lemma 7 weakens, and activations become peakier.

Setup. Let $\mathbf{W}_t \in \mathbb{R}^{d \times d}$ denote a weight matrix at iteration t , and let $\mathbf{G}_t = \nabla_{\mathbf{W}} \mathcal{L}(\mathbf{W}_t)$ be its gradient. We are interested in how the update rule affects the near-isometry condition

$$\mathbf{W}_t \mathbf{W}_t^\top - \mathbf{I} = \mathbf{E}_t, \quad (14)$$

where $\|\mathbf{E}_t\| = \epsilon_t$ is very small.

Spectral GD updates. The spectral-gradient descent update has the form

$$\mathbf{W}_{t+1} = \mathbf{W}_t - \eta \mathbf{U}_t \mathbf{V}_t^\top, \quad (15)$$

where $\mathbf{G}_t = \mathbf{U}_t \mathbf{S}_t \mathbf{V}_t^\top$.

Sign GD updates. The sign-gradient descent update step is

$$\mathbf{W}_{t+1} = \mathbf{W}_t - \eta \text{sign}(\mathbf{G}_t), \quad (16)$$

where $\text{sign}(\mathbf{G}_t)$ is applied entrywise.

Lemma 8 (Spectral gradient descent preserves near-isometry). *Consider the spectral update Eq. (15), and assume \mathbf{W}_t satisfies near-isometry. Then*

$$\|\mathbf{W}_{t+1} \mathbf{W}_{t+1}^\top - \mathbf{I}\|_2 \leq \mathcal{O}(\eta). \quad (17)$$

Proof. Lets evaluate $\mathbf{W}_{t+1} \mathbf{W}_{t+1}^\top$ by expanding the update,

$$\begin{aligned} \mathbf{W}_{t+1} \mathbf{W}_{t+1}^\top - \mathbf{I} &= (\mathbf{W}_t - \eta \mathbf{U}_t \mathbf{V}_t^\top)(\mathbf{W}_t - \eta \mathbf{U}_t \mathbf{V}_t^\top)^\top - \mathbf{I} \\ &= \mathbf{W}_t \mathbf{W}_t^\top - \eta(\mathbf{W}_t \mathbf{V}_t \mathbf{U}_t^\top + \mathbf{U}_t \mathbf{V}_t^\top \mathbf{W}_t^\top) + \eta^2 \mathbf{U}_t \mathbf{V}_t^\top \mathbf{V}_t \mathbf{U}_t^\top - \mathbf{I} \\ &= \mathbf{E}_t - 2\eta \mathbf{W}_t \mathbf{V}_t \mathbf{U}_t^\top + \eta^2 \mathbf{I} \quad ; \mathbf{U}, \mathbf{V}, \mathbf{W} \text{ are orthogonal} \end{aligned}$$

Now the spectral norm can be bounded as,

$$\begin{aligned} \|\mathbf{W}_{t+1} \mathbf{W}_{t+1}^\top - \mathbf{I}\|_2 &\leq \epsilon_t + 2\eta \|\mathbf{W}_t\|_2 \|\mathbf{U}_t \mathbf{V}_t^\top\|_2 + \eta^2 \\ &\leq \epsilon_t + 2\eta + \eta^2 = \mathcal{O}(\eta) \end{aligned}$$

□

Remark 2. *Lemma 8 shows that spectral updates can preserve near-isometry for sufficiently small learning rate. Therefore, they can preserve the dense orthogonal mixing regime needed for the $1/d$ excess kurtosis shrinkage in residual-free networks.*

Now, lets analyze Sign GD updates in a similar fashion.

Lemma 9 (Large operator norm of dense sign updates). *Let $\mathbf{S} \in \{\pm 1\}^{d \times d}$ be a dense sign matrix. Then generically*

$$\|\mathbf{S}\|_2 = \mathcal{O}(\sqrt{d}).$$

Proof. A $d \times d$ random dense sign matrix has the largest singular value of order \sqrt{d} with high probability. The same scaling applies to dense sign patterns. Thus, a dense entrywise sign update has operator norm $\mathcal{O}(\sqrt{d})$ rather than $\mathcal{O}(1)$. □

Substituting this into the $\mathbf{W}_{t+1} \mathbf{W}_{t+1}^\top$ expansion gives much larger drift from identity \mathbf{I} .

Lemma 10 (Sign GD destroys near-isometry faster). *Consider the spectral update Eq. (16), and assume \mathbf{W}_t satisfies near-isometry. Then*

$$\|\mathbf{W}_{t+1} \mathbf{W}_{t+1}^\top - \mathbf{I}\|_2 \leq \mathcal{O}(\eta \sqrt{d} + \eta^2 d), \quad (18)$$

implying sign-like updates can destroy orthogonality much faster than spectral updates.

Proof. Lets evaluate $\mathbf{W}_{t+1}\mathbf{W}_{t+1}^\top$ by expanding the update,

$$\begin{aligned}\mathbf{W}_{t+1}\mathbf{W}_{t+1}^\top - \mathbf{I} &= (\mathbf{W}_t - \eta \text{sign}(\mathbf{G}_t))(\mathbf{W}_t - \eta \text{sign}(\mathbf{G}_t))^\top - \mathbf{I} \\ &= \mathbf{W}_t\mathbf{W}_t^\top - \eta(\mathbf{W}_t \text{sign}(\mathbf{G}_t)^\top + \text{sign}(\mathbf{G}_t)\mathbf{W}_t^\top) + \eta^2 \text{sign}(\mathbf{G}_t) \text{sign}(\mathbf{G}_t)^\top - \mathbf{I} \\ &= \mathbf{E}_t + \eta(\mathbf{W}_t \text{sign}(\mathbf{G}_t)^\top + \text{sign}(\mathbf{G}_t)\mathbf{W}_t^\top) + \eta^2 \text{sign}(\mathbf{G}_t) \text{sign}(\mathbf{G}_t)^\top\end{aligned}$$

Now the spectral norm can be bounded as,

$$\begin{aligned}\|\mathbf{W}_{t+1}\mathbf{W}_{t+1}^\top - \mathbf{I}\|_2 &\leq \epsilon_t + 2\eta\|\mathbf{W}_t\|_2\|\text{sign}(\mathbf{G}_t)\|_2 + \eta^2\|\text{sign}(\mathbf{G}_t)\|_2^2 \\ &\leq \epsilon_t + 2\eta\sqrt{d} + \eta^2d = \mathcal{O}(\eta\sqrt{d} + \eta^2d) \quad ; \|\mathbf{W}_t\|_2 = 1, \text{Lemma 9}\end{aligned}$$

□

Remark 3. Compared to the $O(\eta)$ drift from spectral updates, sign GD exhibits a much larger $O(\eta\sqrt{d} + \eta^2d)$ drift. Hence, in high dimension, sign-like methods can quickly destroy the near-isometric dense-mixing structure, even when the initialization is orthogonal.

C.5 Excess Kurtosis Behavior in Residual Settings

Lemma 11 (Residual addition preserves excess kurtosis (no shrinkage)). *Let \mathbf{x} have i.i.d. centered unit variance coordinates with excess kurtosis γ_x , i.e., $\mathbb{E}[x_i] = 0$, $\mathbb{E}[x_i^2] = 1$ and $\mathbb{E}[x_i^4] = 3 + \gamma_x$.*

Let $\mathbf{W} \in \mathbb{R}^{d \times d}$ have i.i.d. Gaussian entries $\mathcal{N}(0, \frac{1}{d})$ independent of \mathbf{x} . Define the residual update

$$y_j = x_j + \sum_{i=1}^d \phi(x_i)W_{ij},$$

for a fixed coordinate j . Let

$$m_2 = \mathbb{E}[\phi(x)^2], \quad m_4 = \mathbb{E}[\phi(x)^4], \quad c_{22} = \mathbb{E}[x^2\phi(x)^2],$$

where x denotes a generic coordinate distributed as any x_i . Then y_j is centered with variance

$$\text{Var}(y_j) = 1 + m_2,$$

and excess kurtosis

$$\gamma_{y_j} = \frac{3 + \gamma_x + \frac{6}{d}(c_{22} + (d-1)m_2) + \frac{3}{d^2}(dm_4 + d(d-1)m_2^2)}{(1 + m_2)^2} - 3 = \mathcal{O}\left(\gamma_x + \frac{1}{d}\right). \quad (19)$$

Proof. Fix j and define

$$z_j = \sum_{i=1}^d \phi(x_i)W_{ij}.$$

Conditioned on \mathbf{x} , the variable z_j is Gaussian with mean 0 and variance

$$\text{Var}(z_j | \mathbf{x}) = \frac{1}{d} \sum_{i=1}^d \phi(x_i)^2.$$

Let $S = \sum_{i=1}^d \phi(x_i)^2$. Then, conditional on \mathbf{x} ,

$$y_j | \mathbf{x} \sim \mathcal{N}\left(x_j, \frac{S}{d}\right).$$

Hence

$$\mathbb{E}[y_j | \mathbf{x}] = x_j, \quad \mathbb{E}[y_j^2 | \mathbf{x}] = x_j^2 + \frac{S}{d}, \quad \mathbb{E}[y_j^4 | \mathbf{x}] = x_j^4 + 6\frac{S}{d}x_j^2 + 3\frac{S^2}{d^2}.$$

Taking expectation gives

$$\mathbb{E}[y_j] = \mathbb{E}[x_j] = 0.$$

Similarly,

$$\mathbb{E} [y_j^2] = \mathbb{E} [x_j^2] + \frac{1}{d} \mathbb{E} [S].$$

Since the coordinates are i.i.d.,

$$\mathbb{E} [S] = \sum_{i=1}^d \mathbb{E} [\phi(x_i)^2] = dm_2,$$

and therefore

$$\text{Var}(y_j) = \mathbb{E} [y_j^2] = 1 + m_2.$$

For the fourth moment,

$$\mathbb{E} [y_j^4] = \mathbb{E} [x_j^4] + 6 \frac{1}{d} \mathbb{E} [x_j^2 S] + 3 \frac{1}{d^2} \mathbb{E} [S^2].$$

Now $\mathbb{E} [x_j^4] = 3 + \gamma_x$. Also,

$$\begin{aligned} \mathbb{E} [x_j^2 S] &= \mathbb{E} [x_j^2 \phi(x_j)^2] + \sum_{i \neq j} \mathbb{E} [x_j^2 \phi(x_i)^2] \\ &= c_{22} + (d-1) \mathbb{E} [x_j^2] \mathbb{E} [\phi(x_i)^2] = c_{22} + (d-1)m_2. \end{aligned}$$

Finally,

$$\begin{aligned} \mathbb{E} [S^2] &= \mathbb{E} \left[\left(\sum_{i=1}^d \phi(x_i)^2 \right)^2 \right] \\ &= \sum_{i=1}^d \mathbb{E} [\phi(x_i)^4] + \sum_{i \neq r} \mathbb{E} [\phi(x_i)^2 \phi(x_r)^2] \\ &= dm_4 + d(d-1)m_2^2. \end{aligned}$$

Substituting these identities into $\mathbb{E} [y_j^4]$, we obtain

$$\mathbb{E} [y_j^4] = 3 + \gamma_x + \frac{6}{d} (c_{22} + (d-1)m_2) + \frac{3}{d^2} (dm_4 + d(d-1)m_2^2).$$

Therefore

$$\gamma_{y_j} = \frac{\mathbb{E} [y_j^4]}{\text{Var}(y_j)^2} - 3,$$

which gives Eq. (19). □

Remark 4. *Unlike dense orthogonal mixing, the residual update of the form $y = x + \phi(x)\mathbf{W}$ does not average over many coordinates, and therefore does not produce a $1/d$ kurtosis shrinkage. Instead, Eq. (19) shows that the excess kurtosis of y remains $\mathcal{O}(\gamma_x + 1/d)$ since m_2 is $\mathcal{O}(1)$ (Lemma 12). Thus, the non-Gaussianity already present in x is preserved up to a perturbative correction. This explains why residual connections tend to retain and accumulate non-Gaussian activations rather than Gaussianizing them.*

C.6 When Residual-Free Can Remain Near-Gaussian While Residual Transformer Need Not

The previous lemmas show that a dense orthogonal mixing suppresses excess kurtosis by a factor of order $1/d$. We now use this fact to analyze the qualitative difference between residual and residual-free architectures.

At a high level, the residual-free architecture repeatedly *replaces* the current representation by a transformed version. Thus, if each layer contains a sufficiently dense, approximately orthogonal

mixing, then any non-Gaussianity produced at intermediate coordinates is averaged out at the next mixing stage. By contrast, the residual architecture updates the representation by *adding* a new transformed term to the previous state. Consequently, non-Gaussianity already present in the hidden state is carried forward instead of being discarded, and may accumulate across layers (Lemma 3).

We first idealize the residual-free layer as a composition of dense linear mixing and a coordinate-wise nonlinearity. This abstraction captures both the self-attention and MLP blocks at the level needed for our kurtosis analysis.

Theorem 2 (Excess kurtosis shrinkage in residual-free layers). *Consider a residual-free network with hidden states $\{x_\ell\}_{\ell \geq 0}$ satisfying $x_{\ell+1} = \mathbf{W}_\ell \phi_\ell(\text{norm}(x_\ell))$, where:*

1. $\mathbf{W}_\ell \in \mathbb{R}^{d \times d}$ satisfies $\sum_{i=1}^d (\mathbf{W}_\ell)_{ji}^2 = 1$, and $\sum_{i=1}^d (\mathbf{W}_\ell)_{ji}^4 \leq \frac{\mu_\ell}{d}$, and $x_\ell \in \mathbb{R}^d$;
2. ϕ_ℓ acts coordinate-wise;
3. conditional on \mathbf{W}_ℓ , the coordinates of $\phi_\ell(\text{norm}(x_\ell))$ have common excess kurtosis $\tilde{\gamma}_\ell$, and the cross-coordinate dependence is negligible or controlled.

Then each coordinate of $x_{\ell+1}$ has same mean and variance as $\phi(\text{norm}(x_\ell))$, and its excess kurtosis $\gamma_{\ell+1}$ satisfies $|\gamma_{\ell+1}| \leq \frac{\mu_\ell}{d} |\tilde{\gamma}_\ell|$. In particular, if $\sup_\ell \mu_\ell \leq \mu < \infty$ and $|\tilde{\gamma}_\ell| \leq C$ uniformly in ℓ , then $|\gamma_{\ell+1}| \leq \frac{\mu C}{d}$, so the representation remains near-Gaussian in the fourth-moment sense whenever d is large, that is, $\mu C \ll d$.

Proof. Let $v_\ell = \text{norm}(x_\ell)$ and fix a coordinate j of $x_{\ell+1}$. By definition, $(x_{\ell+1})_j = \sum_{i=1}^d (\mathbf{W}_\ell)_{ji} \phi_\ell((v_\ell)_i)$. Since \mathbf{W}_ℓ is orthogonal, it preserves the norm/variance. In the case of layer normalization, the mean is zero and variance is one. Applying Lemma 7 to the vector $\phi_\ell(v_\ell)$ with coefficients $(\mathbf{W}_\ell)_j$ yields $|\gamma_{\ell+1}| \leq \frac{\mu_\ell}{d} |\tilde{\gamma}_\ell|$. The second claim follows immediately if μ_ℓ and $\tilde{\gamma}_\ell$ are uniformly bounded. \square

Remark 5. *Theorem 2 formalizes the mechanism favorable to residual-free transformers. If each layer performs a dense, approximately orthogonal mixing, then even if the nonlinearity creates nonzero excess kurtosis at intermediate coordinates, the next mixing step suppresses it by a factor of order $1/d$. Thus, provided training does not destroy the dense-mixing structure or cause $|\tilde{\gamma}_\ell|$ to grow too rapidly with d , the hidden states remain nearly Gaussian.*

Lemma 12 (Excess kurtosis of ReLU/GELU-like activations is $\mathcal{O}(1)$). *Let $g \sim \mathcal{N}(0, \mathbf{I}) \in \mathbb{R}^d$ and $\phi(g)$ denotes the centered and standardized ReLU-like activations output applied entrywise. Then excess kurtosis of $\phi(g)$ coordinatewise is $\mathcal{O}(1)$ with respect to dimension d .*

Proof. As the activations are applied entrywise, there is no dependence on the dimension d . In the case of ReLU, we can explicitly compute the excess kurtosis using the higher order moments m_k . Since

$$m_1 = \frac{1}{\sqrt{2\pi}}, \quad m_2 = \frac{1}{2}, \quad m_3 = \sqrt{\frac{2}{\pi}}, \quad m_4 = \frac{3}{2},$$

$$\gamma_{\text{ReLU}} \approx 2.4076.$$

Similarly, GELU also induces positive excess kurtosis when applied to Gaussian pre-activations. Numerically, the moments of GELU are $m_1 \approx 0.2821$, $m_2 \approx 0.4252$, $m_3 \approx 0.6751$, $m_4 \approx 1.3047$. Therefore, $\gamma_{\text{GELU}} \approx 3.0847$. \square

Remark 6. *If the normalized preactivations entering a nonlinearity like ReLU/GELU are already approximately Gaussian, then the output excess kurtosis introduced by that nonlinearity can be treated as a fixed constant. However, the nonlinearity itself continually injects non-Gaussianity.*

Excess kurtosis of self-attention. While the previous discussion covers MLP explicitly, it also extends to self-attention block. Let the normalized input be x_ℓ and the output of a token i through self-attention be

$$(x_{\ell+1})_i = \text{softmax} \left(\frac{1}{\sqrt{d}} (x_\ell)_i \mathbf{Q}_\ell \mathbf{K}_\ell^\top (x_\ell)_j^\top \right) (x_\ell)_j \mathbf{V}_\ell \mathbf{O}_\ell,$$

where $(\mathbf{x}_\ell)_i$ is the ℓ -th layer representation of token i , $\mathbf{Q}_\ell, \mathbf{K}_\ell, \mathbf{V}_\ell, \mathbf{O}_\ell$ are weight matrices of layer ℓ that satisfy dense orthogonal condition in Theorem 2. The key point is that orthogonality in the attention projections through \mathbf{Q}_ℓ and \mathbf{K}_ℓ controls both the scale of the attention scores and the isotropy of the latter projections through \mathbf{V}_ℓ and \mathbf{O}_ℓ . Together, these effects help maintain near-Gaussian activations. If the excess kurtosis of softmax output is controlled, then the output $\mathbf{x}_{\ell+1}$ is also near-Gaussian due to the orthogonality of \mathbf{V}_ℓ and \mathbf{O}_ℓ . Therefore, the only thing left to be analyzed is the excess kurtosis induced by softmax, whether it increases or shrinks, similar to ReLU/GELU.

Lemma 13 (Excess kurtosis of softmax activation can be $\mathcal{O}(d)$). *Let $\mathbf{g} \sim \mathcal{N}(0, \mathbf{I}) \in \mathbb{R}^d$ and $\mathbf{y} = \text{softmax}(\tau \mathbf{g})$ denotes the softmax activation for some scale parameter $\tau > 0$, that is*

$$y_j = \frac{\exp(\tau g_j)}{\sum_{i=1}^d \exp(\tau g_i)}.$$

Then excess kurtosis of y_j coordinatewise is not dimension independent in general:

1. *in the non-saturated regime, it is $\mathcal{O}(1)$;*
2. *in the saturated regime, it is $\mathcal{O}(d)$.*

Hence the excess kurtosis of a softmax coordinate is controlled only when the logits remain in a non-peaky regime.

Proof. The key distinction is whether the logits τg_j are small enough that softmax behaves approximately linearly, or large enough that softmax is close to an argmax selector/one-hot vector.

In the non-saturated regime, first-order Taylor's approximation of softmax around $\mathbf{0}$ vector gives

$$y_j \approx \frac{1}{d} + \frac{\tau}{d} \left(g_j - \frac{1}{d} \left(\sum_{i=1}^d g_i \right) \right).$$

The centered y_j is $\approx \frac{\tau}{d} g_j$ which is approximately Gaussian. Therefore, its excess kurtosis is $\mathcal{O}(1)$.

In the saturated case, softmax becomes a nearly one-hot vector. Therefore, the coordinates are either 1 with probability $\frac{1}{d}$ or 0 with probability $1 - \frac{1}{d}$. Therefore, a Bernoulli random variable. A Bernoulli random variable with parameter p has excess kurtosis $\frac{1-6p(1-p)}{p(1-p)}$. Hence, in the case of softmax, the excess kurtosis is

$$\frac{d^2 - 6d + 6}{d - 1} = \mathcal{O}(d).$$

Therefore, in the saturated regime, the coordinatewise excess kurtosis of softmax can grow linearly with the softmax dimension d . \square

Remark 7. *Unlike ReLU/GELU-like activations, softmax is not applied entrywise and its kurtosis behavior depends on the geometry of the whole logit vector. If the attention scores remain controlled, then each softmax coordinate behaves like a smooth perturbation of $1/d$ and has $\mathcal{O}(1)$ excess kurtosis. However, if the scores become too large, softmax saturates, the attention weights become peaky, and the coordinatewise excess kurtosis can increase to $\mathcal{O}(d)$. Thus, for attention, controlling the score variance is essential to prevent softmax from becoming a source of strong non-Gaussianity.*

Lemma 14 (Orthogonal $\mathbf{Q}_\ell, \mathbf{K}_\ell$ do not amplify normalized attention scores and controls scale). *Let's consider $\mathbf{Q}_\ell, \mathbf{K}_\ell$ to be orthogonal and the input to softmax,*

$$(\mathbf{s}_\ell)_{ij} = \frac{1}{\sqrt{d}} (\mathbf{x}_\ell)_i \mathbf{Q}_\ell \mathbf{K}_\ell^\top (\mathbf{x}_\ell)_j^\top.$$

The token representations entering attention are centered and variance-controlled through the normalization norm(\cdot), thus their covariance operators satisfy

$$\|\Sigma_{\ell,i}\|_2 = \mathbb{E} [\|(\mathbf{x}_\ell)_i\|_2^2] \leq C, \quad \forall i \tag{20}$$

for a constant C independent of d . Note that $C = 1$ in the case of Layer Normalization. Then $\text{Var}((\mathbf{s}_\ell)_{ij}) = \mathcal{O}(1)$. Consequently, the row-wise softmax operates in a non-saturated regime, and its coordinatewise excess kurtosis remains $\mathcal{O}(1)$.

Proof. Let $\mathbf{M}_\ell = \mathbf{Q}_\ell \mathbf{K}_\ell^\top$. Then $(s_\ell)_{ij} = \frac{1}{\sqrt{d}}(\mathbf{x}_\ell)_i \mathbf{M}_\ell (\mathbf{x}_\ell)_j^\top$. Since $(\mathbf{x}_\ell)_i$ and $(\mathbf{x}_\ell)_j$ are centered, $\mathbb{E}[(s_\ell)_{ij}] = 0$, and hence

$$\begin{aligned}
\text{Var}\left((s_\ell)_{ij}\right) &= \frac{1}{d} \mathbb{E} \left[\left((\mathbf{x}_\ell)_i \mathbf{M}_\ell (\mathbf{x}_\ell)_j^\top \right)^2 \right] \\
&= \frac{1}{d} \mathbb{E} \left[\text{tr} \left((\mathbf{x}_\ell)_i \mathbf{M}_\ell (\mathbf{x}_\ell)_j^\top (\mathbf{x}_\ell)_j \mathbf{M}_\ell (\mathbf{x}_\ell)_i^\top \right) \right] \\
&= \frac{1}{d} \mathbb{E} \left[\text{tr} \left((\mathbf{x}_\ell)_i^\top (\mathbf{x}_\ell)_i \mathbf{M}_\ell (\mathbf{x}_\ell)_j^\top (\mathbf{x}_\ell)_j \mathbf{M}_\ell \right) \right] \\
&= \frac{1}{d} \text{tr} \left(\mathbb{E} \left[(\mathbf{x}_\ell)_i^\top (\mathbf{x}_\ell)_i \mathbf{M}_\ell (\mathbf{x}_\ell)_j^\top (\mathbf{x}_\ell)_j \mathbf{M}_\ell \right] \right) \\
&\leq \frac{1}{d} \mathbb{E} \left[\|\mathbf{x}_\ell\|_2^2 \right] \text{tr} \left(\mathbf{M}_\ell \mathbb{E} \left[(\mathbf{x}_\ell)_j^\top (\mathbf{x}_\ell)_j \right] \mathbf{M}_\ell \right) \\
&\leq \frac{1}{d} \|\Sigma_{\ell,i}\|_2 \|\Sigma_{\ell,j}\|_2 \text{tr} \left(\mathbf{M}_\ell^\top \mathbf{M}_\ell \right) \quad ; \mathbf{M}_\ell^\top \mathbf{M}_\ell = \mathbf{I} \\
&\leq C^2 = \mathcal{O}(1)
\end{aligned}$$

Thus, if the input to the attention block is already normalized or otherwise controlled so that the raw score scale is stable, then the projected attention scores remain stable as well. In particular, the logits do not systematically blow up with dimension, so the softmax remains away from the saturated nearly one-hot regime. By Lemma 13, this implies that each softmax coordinate has $\mathcal{O}(1)$ excess kurtosis. This proves the claim. \square

Remark 8. *The main role of orthogonal \mathbf{Q}_ℓ and \mathbf{K}_ℓ is not to make the softmax output exactly Gaussian, but to prevent the attention scores from entering the peaky saturated regime. Once the score variance is controlled at $\mathcal{O}(1)$ scale, the softmax coordinates remain in the benign regime where their excess kurtosis is also $\mathcal{O}(1)$ rather than growing with the sequence length.*

The preceding analysis explains the empirical behavior observed in the residual-free setting. The key mechanism is that, in the absence of residual addition, each layer *replaces* the current representation by a newly mixed representation rather than carrying forward the previous hidden state. As a result, whether activations remain close to Gaussian is determined by two interacting properties: (i) whether the layer map performs dense near-isometric mixing, and (ii) whether optimization preserves this structure over training.

First, orthogonal initialization is favorable because it induces dense norm-preserving mixing. By Lemma 7, such mixing suppresses excess kurtosis by a factor of order $1/d$. Thus, although nonlinearities such as ReLU, GeLU, and softmax can inject $\mathcal{O}(1)$ non-Gaussianity locally, the next orthogonal mixing step averages this out and keeps the activations close to Gaussian. In attention, orthogonal \mathbf{Q}_ℓ , \mathbf{K}_ℓ control the score variance and prevent softmax saturation, while orthogonal \mathbf{V}_ℓ and \mathbf{O}_ℓ preserve isotropy after softmax. Altogether, this makes the residual-free block behave as a stable averaging-and-mixing operator.

Second, spectral optimizers complement this by preserving the near-isometric structure during training. By Lemma 8, their orthogonality deviation is only $\mathcal{O}(\eta)$, so an initially orthogonal weight matrix remains close to orthogonal for small learning rate. Hence the dense-mixing Gaussianization mechanism continues to hold throughout training. By contrast, default initialization does not enforce isometry. Although activations may be locally Gaussian at initialization, variance is not preserved uniformly across directions, so anisotropy can accumulate across layers. Similarly, sign GD or Adam/AdamW deviates substantially from orthogonality (Lemma 10) even when training starts from an orthogonal initialization, leading to more concentrated coordinate directions and weakening the kurtosis shrinkage.

Taken together, the analysis yields the following result for residual-free transformers.

1. Orthogonal initialization provides the correct geometric starting point by enforcing dense norm-preserving mixing;
2. spectral optimization preserves this geometry over training.

Either ingredient alone is insufficient. Therefore, among the settings considered, the combination of **residual-free + orthogonal initialization + spectral optimization** is the one that naturally maintains near-Gaussian activations.

Interpretation of theorems. Putting everything together yields the following interpretation of the theorems.

1. In **residual-free transformers**, if the learned attention and MLP maps remain sufficiently dense and approximately orthogonal, then each layer re-mixes coordinates and suppresses excess kurtosis introduced by nonlinearities. This creates a self-correcting fourth-moment mechanism toward Gaussian-like activations.
2. In **residual transformers**, the residual stream carries previous non-Gaussianity forward. Even if the branch output were itself close to Gaussian, the sum need not become more Gaussian because the old hidden state is preserved rather than replaced.
3. Between **spectral gradient descent** and sign gradient descent, spectral GD is more likely to preserve dense orthogonal mixing, and sign GD is coordinatewise and weakens $1/d$ kurtosis contraction.
4. Consequently, the combination of **orthogonal initialization** and **spectral optimizers** is especially favorable in the residual-free setting. It both promotes dense norm-preserving mixing at initialization and tends to preserve it during training.

D Experimental Details

We use LLaMA-style decoder-only transformers with GELU activations in the feedforward blocks. All models are pretrained on FineWeb-Edu [Penedo et al., 2024] for 50k steps using the next-token prediction objective. The models have 24 layers with hidden dimension 768 and 12 attention heads, totaling 194 million parameters. We use LlamaTokenizer and 32000 vocab size. We use a batch size of 512 sequences, sequence length 512, and 2k warmup steps. Unless otherwise specified, weight decay is set to 0.01. For residual-free models, we use the orthogonal initialization described in Section 4, with $\alpha_{QK} = 0.9$, $\alpha_{VO} = 3$ and $\alpha_U = \alpha_D = 1.5$. For depth-aware attention temperature scaling, we use base scaling factor $\beta = 1.1$. We sweep learning rates in the range $[1e-4, 5e-3]$ and report results using the best stable setting for each optimizer and architecture. The selected learning rates are:

- Residual + AdamW is $1e-3$.
- Residual + KL Shampoo is $1e-3$
- Residual-free + KL Shampoo is $5e-4$.
- Residual-free + Muon is $7e-4$.
- Residual-free + SOAP is $5e-4$.

Quantization protocol. After pretraining, we quantize tensors from full precision (BF16) to integer formats. Unless otherwise stated, we apply simple uniform quantization to both weights and activations, without any additional outlier handling, reconstruction, or learned rotations. This choice is intentional: our goal is to measure the intrinsic quantization robustness of the activation distributions produced by different architectures and optimizers. We adopt the notation W_nA_m to denote n -bit weight quantization and m -bit activation quantization (e.g., W_8A_{12} corresponds to 8-bit weights and 12-bit activations). Weights are quantized first, followed by activations. Since our focus is activation outliers, we quantize activations at the inputs to the normalization layers and the SA/MLP. For weights, we use per-channel asymmetric static quantization; for activations, we use per-tensor quantization. The calibration set consists of 32k tokens sampled from FineWeb-Edu.

Evaluation metrics. For activation Gaussianity, we report excess kurtosis as defined in Definition 1. We additionally measure negentropy, a standard information-theoretic proxy for non-Gaussianity.

Definition 3 (Negentropy). For a random variable x with covariance matched to a Gaussian random variable g , negentropy is

$$J(x) = H(g) - H(x),$$

where $H(\cdot)$ denotes differential entropy.

Since a Gaussian maximizes entropy among distributions with fixed covariance, $J(x) \geq 0$, with equality only for a Gaussian distribution.

For quantization, we report downstream accuracy after quantizing weights and activations to integer formats. We also compute normalized mean-squared error (MSE) and signal-to-quantization-noise ratio (SQNR) between full-precision tensors x and their quantized-original versions \hat{x} :

$$\text{Normalized MSE}(x, \hat{x}) = \frac{\|x - \hat{x}\|_2^2}{\|x\|_2^2}, \quad \text{SQNR}(x, \hat{x}) = 10 \log_{10} \left(\frac{\|x\|_2^2}{\|x - \hat{x}\|_2^2} \right).$$

Downstream evaluation. We evaluate pretrained language models on eight zero-shot common-sense reasoning benchmarks: *arc_c*, *arc_e*, *boolq*, *hellaswag*, *openbookqa*, *piqa*, *social_iqa*, and *wino grande*. We report task accuracy and the average accuracy across all tasks. We do not report training-seed error bars due to the cost of pretraining, but we provide per-task results and tensor-level distortion metrics to support the average trends. Also, because zero-shot task accuracy is noisy and quantization can perturb answer rankings non-monotonically on individual tasks, we focus on average trends across tasks and complement accuracy with tensor-level SQNR/MSE.

Hardware. Each experiment is run on 4 H100 GPUs. For Residual with KL Shampoo, it takes 90622 MB memory on each GPU and 1.56 steps per second. For Residual with Adamw, it takes 90328 MB memory on each GPU and 4.77 steps per second. For Residual-Free with KL Shampoo, it takes 81598 MB of memory on each GPU and 1.7 steps per second. For Residual-Free with SOAP, it takes 81596 MB memory on each GPU and 0.9 steps per second. For Residual-Free with MUON, it takes 81304 MB memory and 4.6 steps per second.

Code. A functioning code repository is provided as a zip file in the supplementary material.

E Additional Experiments

In this section, we provide additional empirical evidence supporting the statistical and quantization advantages of residual-free transformers.

E.1 Residual-free Transformers With Second-Order Optimizations

We study how different optimizers affect the activation statistics of residual-free transformers. Figure 5 shows that residual-free models when trained with second order optimizers result in activations that have near-zero excess kurtosis and negentropy, indicating Gaussian-like behavior under these diagnostics. We further illustrate the activation histograms of all residual-free models trained with different second-order optimizers for layers 8, 16, and 22 after 50k steps in Figure 6, which confirms the well-concentrated, symmetric distributions with very low excess kurtosis, matching near-Gaussian distributions.

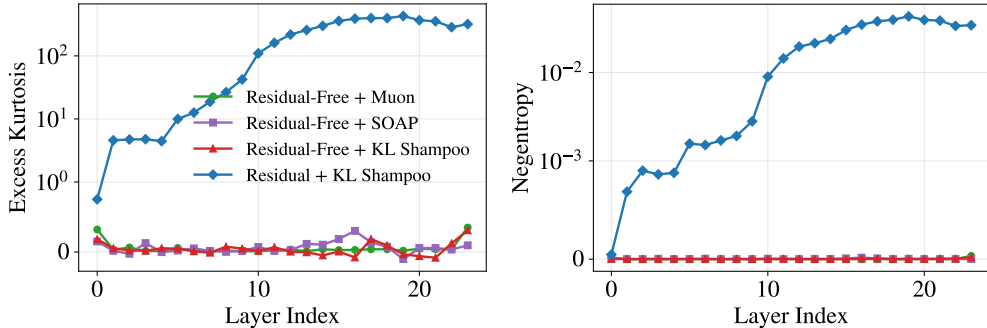


Figure 5: Excess kurtosis and negentropy comparison of residual-free models pretrained with different optimizers and a residual model trained with KL Shampoo. Residual-free models show near-zero excess kurtosis and negentropy, therefore near-Gaussian activations.

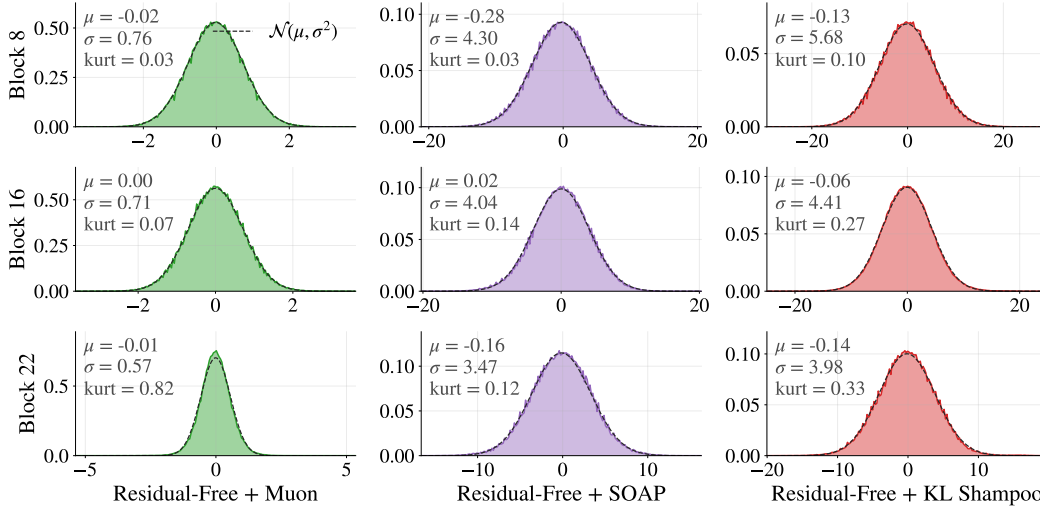


Figure 6: Activation distribution comparison of residual-free models pretrained with different second-order optimizers, such as Muon, SOAP, KL Shampoo, at steps 50k step. All models produce near-Gaussian activations, with low excess kurtosis across depth.

E.2 Residual and Residual-Free Transformers: Activation Distribution

We now illustrate the distribution of activations during training for residual and residual-free models. Figures 7 to 9 show the evolution of activation distributions during training across residual models trained with AdamW and KL Shampoo, and residual with KL Shampoo for layers 8, 16, and 22, respectively.

- Consistently, the residual model with KL Shampoo maintains near-Gaussian activations across layers and across training steps.
- AdamW rapidly loses Gaussianity during training and becomes extremely peaky across layers, with excess kurtosis decreasing across layers. That is, distributions peak throughout training, the peaking is high in initial layers. For instance, in 50k step, the excess kurtosis decreases from 73,998 to 40,527 to 553. While they all remain non-Gaussian, this shows the earlier layers far more peaky and difficult to quantize, which is also evident from their value ranges.
- In the case of residual and KL Shampoo, it also becomes non-Gaussian similar to AdamW, but it is more gradual during training. Across layers, it maintains similar excess kurtosis, suggesting that it can be due to the isometry updates of spectral type optimizations.

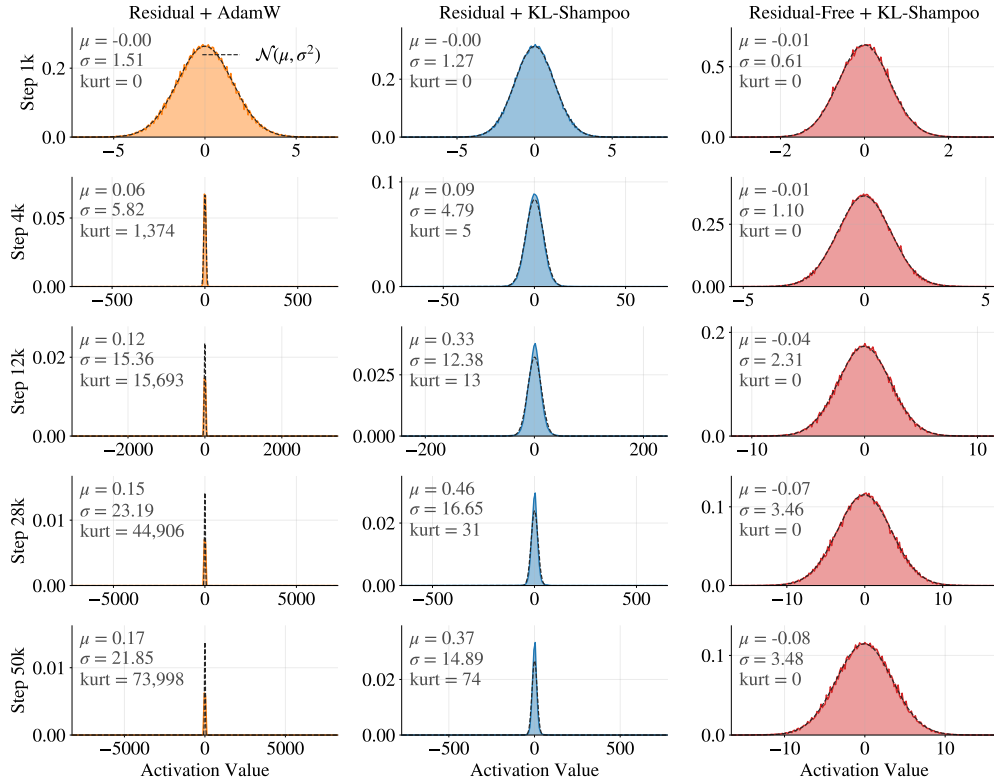


Figure 7: Activation distribution comparison of residual and residual-free for layer 8 during training.

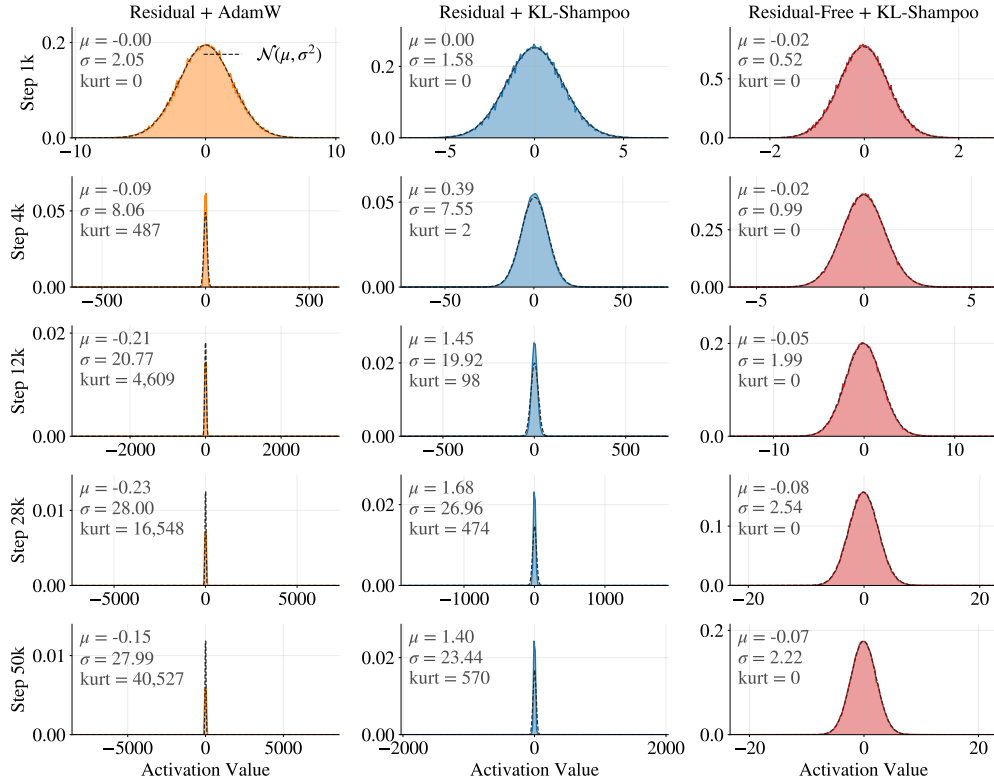


Figure 8: Activation distribution comparison of residual and residual-free for layer 16 during training.

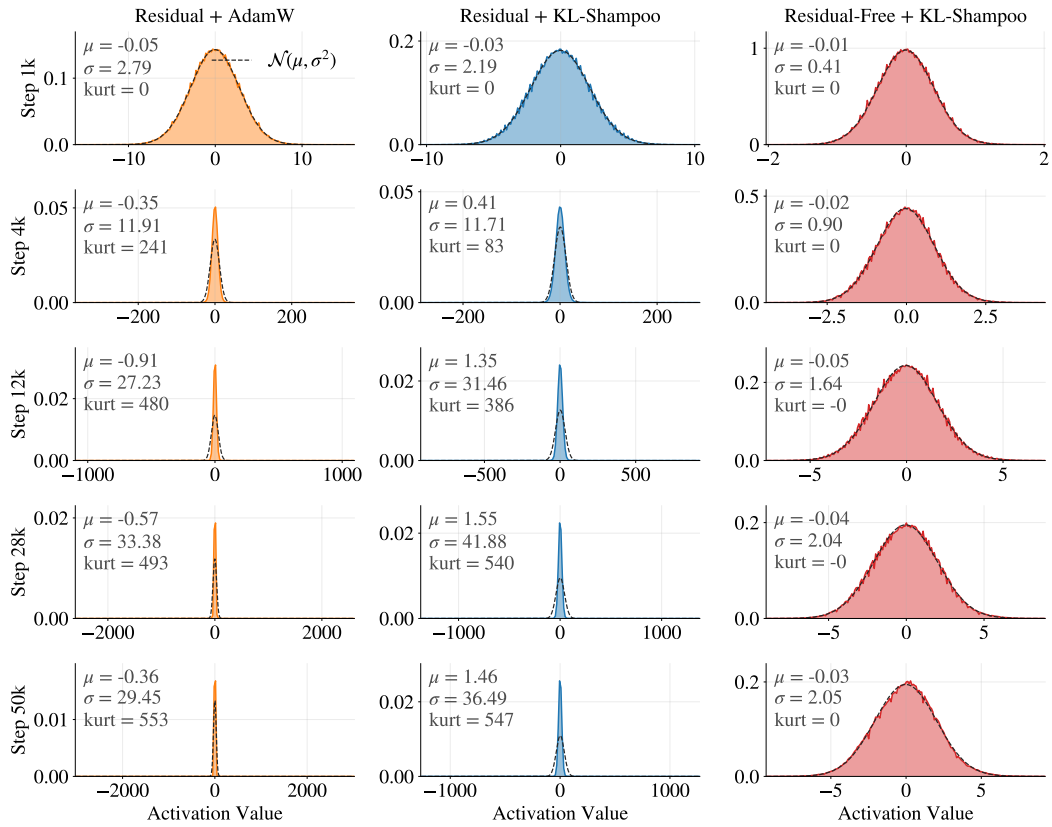


Figure 9: Activation distribution comparison of residual and residual-free for layer 22 during training.

E.3 Residual and Residual-Free Transformers: W8 Quantization Results

We further analyze the relationship between activation statistics and quantization performance across different precisions, focusing on 8-bit quantization of weights in this section. Figure 10 shows that residual-free models maintain stable accuracy even at low activation bit-widths, while residual models degrade significantly, especially when trained with AdamW. This behavior is consistent with the distortion metrics in Figure 11, where residual-free models achieve higher SQNR and substantially lower normalized MSE across all bit-widths. The improvement is particularly pronounced at 4–8 bits, where quantization error is most sensitive to activation outliers. Finally, the layerwise statistics confirm the underlying mechanism that residual-free models maintain near-zero excess kurtosis and negentropy across depth, while residual models accumulate heavy-tailed, non-Gaussian activations, leading to higher quantization error. Table 2 shows the complete results.

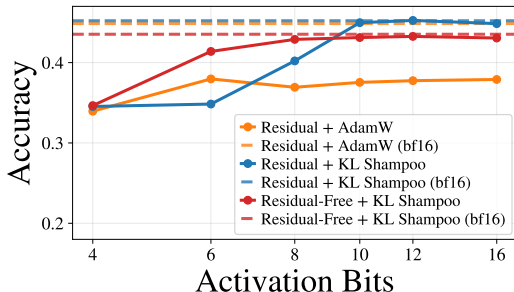


Figure 10: Accuracy as a function of activation bit-width and 8-bit weights. Residual-free transformers maintain stable performance even at low precision, while residual models exhibit significant degradation, particularly when trained with AdamW. Dashed lines indicate full-precision (BF16) baselines.

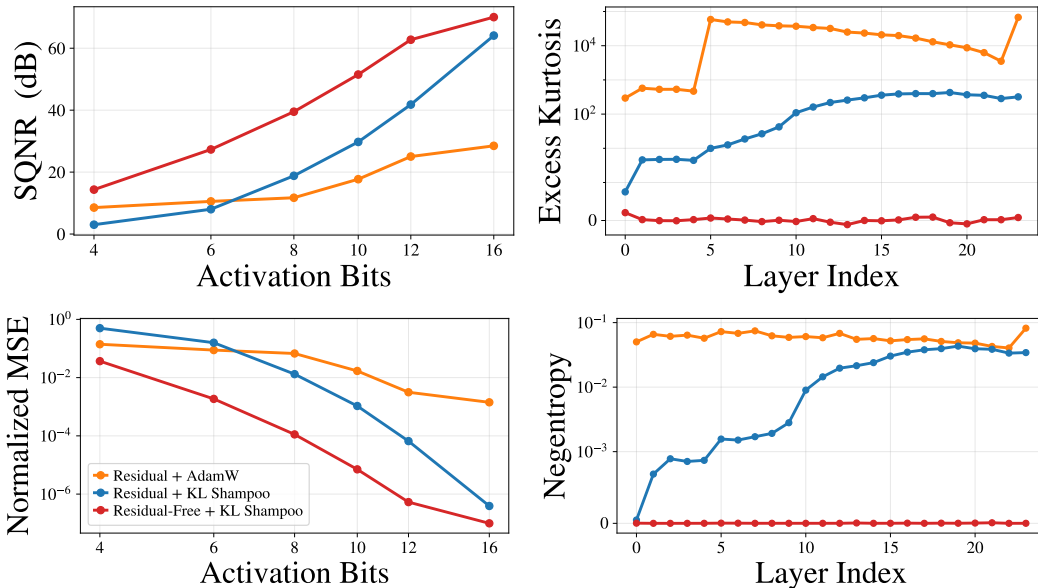


Figure 11: Quantization distortion and activation statistics. **Top-left:** SQNR improves steadily with bit-width, with residual-free models achieving the highest signal fidelity. **Bottom-left:** normalized MSE decreases significantly faster for residual-free models, especially at low precision. **Right:** layerwise excess kurtosis and negentropy show that residual models accumulate heavy-tailed, non-Gaussian activations, while residual-free models remain close to Gaussian. These statistical differences explain the improved quantization robustness.

Table 2: **Residual-free transformers are substantially quantization robust.** Zero-shot performance (average accuracy) on 8 downstream tasks comparison across models under different quantization configurations.

Model	Quantization	arc_c	arc_e	boolq	hellaswag	openbookqa	piqa	social_iqa	winogrande	avg
Residual AdamW	BF16	0.257	0.488	0.583	0.370	0.330	0.653	0.383	0.524	0.449
	W8A16	0.230	0.367	0.476	0.291	0.262	0.545	0.347	0.513	0.379
	W8A12	0.232	0.334	0.500	0.295	0.264	0.526	0.347	0.521	0.378
	W8A10	0.230	0.343	0.495	0.290	0.268	0.529	0.348	0.500	0.375
	W8A8	0.273	0.284	0.507	0.263	0.272	0.500	0.346	0.510	0.369
	W8A6	0.279	0.262	0.619	0.263	0.272	0.503	0.326	0.515	0.380
	W8A4	0.272	0.261	0.380	0.258	0.240	0.487	0.343	0.475	0.340
Residual KL Shampoo	BF16	0.265	0.513	0.582	0.385	0.312	0.650	0.396	0.514	0.452
	W8A16	0.255	0.509	0.595	0.374	0.304	0.640	0.388	0.522	0.449
	W8A12	0.265	0.510	0.596	0.377	0.318	0.641	0.387	0.526	0.453
	W8A10	0.271	0.509	0.588	0.375	0.310	0.631	0.390	0.523	0.450
	W8A8	0.222	0.401	0.578	0.311	0.270	0.565	0.349	0.521	0.402
	W8A6	0.277	0.263	0.380	0.258	0.244	0.505	0.348	0.513	0.348
	W8A4	0.286	0.258	0.382	0.253	0.238	0.492	0.343	0.511	0.345
Residual-Free KL Shampoo	BF16	0.257	0.463	0.606	0.343	0.316	0.616	0.371	0.511	0.435
	W8A16	0.245	0.454	0.587	0.345	0.302	0.616	0.369	0.526	0.431
	W8A12	0.252	0.450	0.589	0.345	0.318	0.617	0.366	0.524	0.433
	W8A10	0.241	0.460	0.585	0.343	0.326	0.618	0.361	0.515	0.431
	W8A8	0.247	0.448	0.590	0.344	0.292	0.611	0.370	0.529	0.429
	W8A6	0.243	0.415	0.553	0.331	0.296	0.582	0.366	0.527	0.414
	W8A4	0.272	0.269	0.394	0.260	0.238	0.497	0.342	0.500	0.346

E.4 Residual and Residual-Free Transformers: W16 Quantization Results

Similar to the previous section, we do 16-bit quantization of weights and analyze the performance of residual and residual free models. The results are consistent with 8-bit weight quantization. Figure 12 shows that residual-free models maintain stable accuracy even at low activation bit-widths, while residual models degrade significantly, especially when trained with AdamW. This behavior is consistent with the distortion metrics in Figure 13, where residual-free models achieve higher SQNR and substantially lower normalized MSE across all bit-widths, along with confirming layerwise excess kurtosis and negentropy. Table 3 shows the complete results.

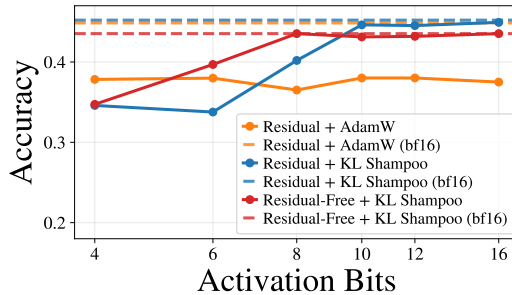


Figure 12: Accuracy as a function of activation bit-width and 16-bit weights. Residual-free transformers maintain stable performance even at low precision, while residual models exhibit significant degradation, particularly when trained with AdamW. Dashed lines indicate full-precision (BF16) baselines.

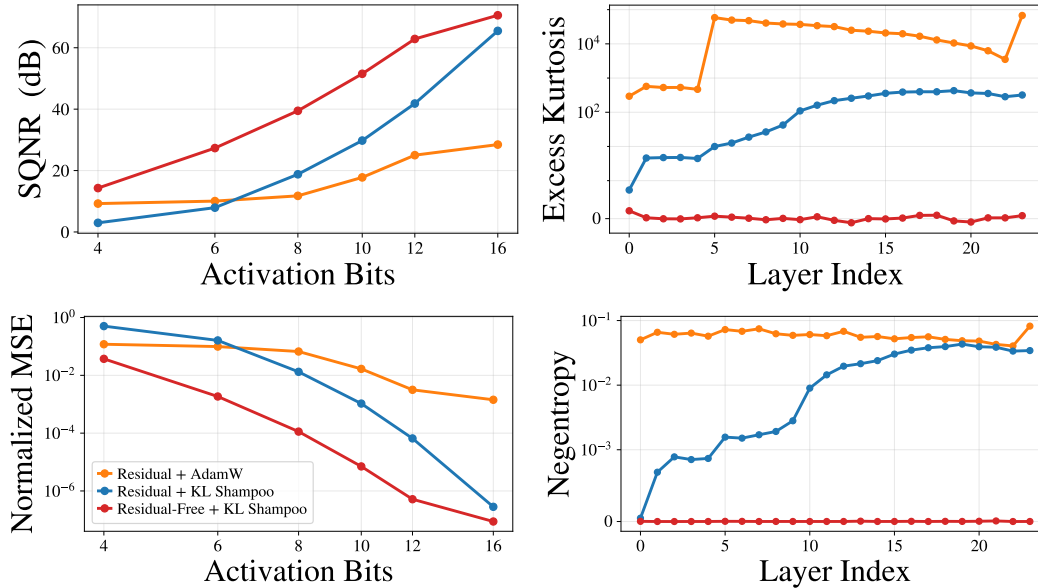


Figure 13: Quantization distortion and activation statistics. **Top-left:** SQNR improves steadily with bit-width, with residual-free models achieving the highest signal fidelity. **Bottom-left:** normalized MSE decreases significantly faster for residual-free models, especially at low precision. **Right:** layerwise excess kurtosis and negentropy show that residual models accumulate heavy-tailed, non-Gaussian activations, while residual-free models remain close to Gaussian. These statistical differences explain the improved quantization robustness.

Table 3: **Residual-free transformers are substantially quantization robust.** Zero-shot performance (average accuracy) on 8 downstream tasks comparison across models under different quantization configurations.

Model	Quantization	arc_c	arc_e	boolq	hellaswag	openbookqa	piqa	social_iqa	winogrande	avg
Residual AdamW	BF16	0.257	0.488	0.583	0.370	0.330	0.653	0.383	0.524	0.449
	W16A16	0.231	0.347	0.471	0.290	0.262	0.542	0.346	0.510	0.375
	W16A12	0.231	0.338	0.542	0.288	0.240	0.549	0.346	0.507	0.380
	W16A10	0.229	0.372	0.478	0.287	0.276	0.537	0.344	0.518	0.380
	W16A8	0.260	0.278	0.489	0.260	0.264	0.504	0.351	0.515	0.365
	W16A6	0.285	0.269	0.614	0.265	0.266	0.496	0.337	0.507	0.380
	W16A4	0.282	0.259	0.621	0.264	0.264	0.496	0.342	0.499	0.378
Residual KL Shampoo	BF16	0.265	0.513	0.582	0.385	0.312	0.650	0.396	0.514	0.452
	W16A16	0.262	0.478	0.609	0.356	0.318	0.637	0.385	0.511	0.445
	W16A12	0.265	0.479	0.609	0.352	0.322	0.636	0.380	0.517	0.445
	W16A10	0.259	0.469	0.595	0.352	0.304	0.635	0.369	0.510	0.437
	W16A8	0.207	0.388	0.485	0.301	0.292	0.557	0.349	0.517	0.387
	W16A6	0.271	0.274	0.392	0.263	0.260	0.492	0.354	0.493	0.350
	W16A4	0.295	0.263	0.382	0.254	0.242	0.520	0.344	0.511	0.351
Residual-Free KL Shampoo	BF16	0.257	0.463	0.606	0.343	0.316	0.616	0.371	0.511	0.435
	W16A16	0.254	0.458	0.600	0.342	0.312	0.619	0.371	0.526	0.435
	W16A12	0.252	0.457	0.595	0.342	0.316	0.614	0.374	0.504	0.432
	W16A10	0.261	0.460	0.594	0.340	0.300	0.619	0.377	0.500	0.431
	W16A8	0.265	0.459	0.607	0.344	0.312	0.618	0.376	0.503	0.435
	W16A6	0.241	0.389	0.498	0.313	0.278	0.579	0.356	0.522	0.397
	W16A4	0.271	0.268	0.418	0.256	0.238	0.505	0.333	0.490	0.347

E.5 Residual and Residual-Free Transformers: Weight Full Precision Quantization Results

In this section, we do not quantize weights and analyze the performance of residual and residual-free models only under activation quantization. The results are interestingly consistent with full precision weights. Figure 14 shows that residual-free models maintain stable accuracy even at low activation bit-widths, while residual models degrade significantly, especially when trained with AdamW. This behavior is consistent with the distortion metrics in Figure 15, where residual-free models achieve higher SQNR and substantially lower normalized MSE across all bit-widths, along with confirming layerwise excess kurtosis and negentropy. The evaluations across different weight quantization suggest that activation quantization affects the performance much more significantly than weight quantization, as the performances are similar, for example, A8, W8A8, and W16A8.

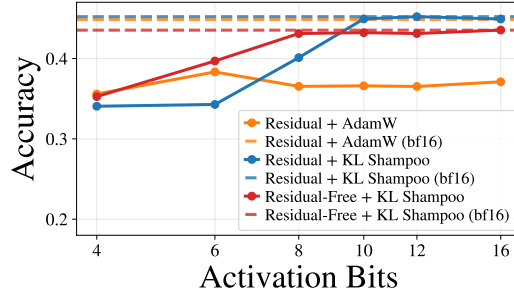


Figure 14: Accuracy as a function of activation bit-width and full precision. Residual-free transformers maintain stable performance even at low precision, while residual models exhibit significant degradation, particularly when trained with AdamW. Dashed lines indicate full-precision (BF16) baselines.

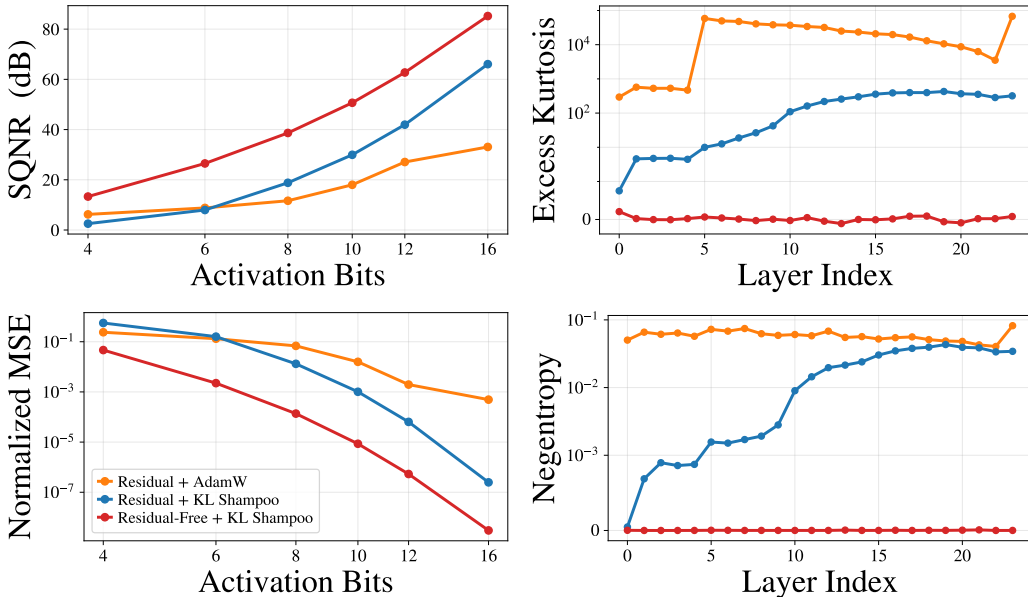


Figure 15: Quantization distortion and activation statistics. **Top-left:** SQNR improves steadily with bit-width, with residual-free models achieving the highest signal fidelity. **Bottom-left:** normalized MSE decreases significantly faster for residual-free models, especially at low precision. **Right:** layerwise excess kurtosis and negentropy show that residual models accumulate heavy-tailed, non-Gaussian activations, while residual-free models remain close to Gaussian. These statistical differences explain the improved quantization robustness.

Table 4: Zero-shot performance (Accuracy %) on 8 downstream tasks under *activation-only* quantization (weights kept in BF16).

Model	Quantization	arc_c	arc_e	boolq	hellaswag	openbookqa	piqa	social_iqa	winogrande	avg
Residual AdamW	BF16	0.257	0.488	0.583	0.370	0.330	0.653	0.383	0.524	0.449
	A16	0.219	0.348	0.460	0.285	0.254	0.550	0.341	0.511	0.371
	A12	0.241	0.342	0.402	0.280	0.268	0.529	0.354	0.506	0.365
	A10	0.216	0.355	0.449	0.289	0.254	0.526	0.341	0.498	0.366
	A8	0.271	0.274	0.487	0.263	0.276	0.495	0.352	0.504	0.365
	A6	0.278	0.265	0.621	0.264	0.280	0.492	0.339	0.527	0.383
	A4	0.285	0.252	0.476	0.252	0.262	0.487	0.343	0.490	0.356
Residual KL Shampoo	BF16	0.265	0.513	0.582	0.385	0.312	0.650	0.396	0.514	0.452
	A16	0.266	0.509	0.589	0.376	0.312	0.638	0.387	0.516	0.449
	A12	0.271	0.508	0.590	0.378	0.318	0.640	0.379	0.533	0.452
	A10	0.269	0.498	0.588	0.378	0.330	0.640	0.380	0.511	0.449
	A8	0.213	0.423	0.575	0.310	0.280	0.574	0.346	0.488	0.401
	A6	0.274	0.265	0.381	0.259	0.228	0.503	0.342	0.491	0.343
	A4	0.267	0.266	0.380	0.251	0.234	0.493	0.347	0.487	0.341
Residual-Free KL Shampoo	BF16	0.257	0.463	0.606	0.343	0.316	0.616	0.371	0.511	0.435
	A16	0.259	0.460	0.601	0.343	0.314	0.616	0.375	0.515	0.435
	A12	0.247	0.457	0.601	0.344	0.310	0.619	0.370	0.503	0.431
	A10	0.252	0.457	0.604	0.341	0.308	0.621	0.366	0.508	0.432
	A8	0.247	0.456	0.610	0.342	0.308	0.610	0.369	0.505	0.431
	A6	0.235	0.385	0.545	0.309	0.258	0.565	0.357	0.521	0.397
	A4	0.300	0.270	0.415	0.262	0.234	0.499	0.339	0.501	0.353

F Broader Impact Statement

This work studies how architectural choices influence activation statistics and their implications for low-bit quantization. By enabling more effective use of simple uniform quantization, our approach can reduce the memory and bandwidth requirements of large-scale models, potentially making training and deployment more environmentally efficient. At the same time, lowering deployment costs may accelerate both beneficial and harmful uses of foundation models. Our work does not directly address issues such as misuse, fairness, or safety, as our focus is foundational understanding of these models. Thus, we believe the potential benefits of robustness research outweigh its risks. Additionally, we do not see any immediate risk stemming from our work.